Chapter 2

Time-Distance Helioseismology: Observations [1]

[1]This chapter is essentially a compilation of articles that appeared in Solar Physics (Duvall & Gizon, 2000), Nature (Gizon et al., 2003), the Astrophysical Journal (Beck et al., 2002), and the proceedings of the IAU Symposium 203 (Gizon et al., 2001b) and of the SOHO 12 conference(Hindman et al., 2003; Gizon & Duvall, 2003). Although I did the final analysis of the travel-times in all cases, many people contributed to these observations. The cross-correlations were computed using the code of Tom Duvall, except for § 2.6. John Beck computed the cross-correlations in § 2.6 using Peter Giles' code. Tom Duvall did part of the writing in § 2.1, Brad Hindman in § 2.5 and John Beck in § 2.6. Useful discussions with Jesper Schou and Douglas Gough are acknowledged.

2.1 Time-Distance Helioseismology with f Modes

In this introductory section, we demonstrate the utility of f-mode time-distance helioseismology. Travel times measured for the f mode have been used to study flows near the solar surface in conjunction with simultaneous measurements of the magnetic field. We measure the spatial and temporal power spectra of the supergranular flows for a six-day observing sequence. Previous measurements of Doppler surface rotation, small magnetic feature rotation, supergranular pattern rotation, and surface meridional circulation are confirmed and compared to the f-mode measurements.

2.1.1 Introduction

The fundamental, or f, modes are classified as surface gravity waves with very nearly the classical water-wave dispersion relation, $\omega^2 = gk$, where ω is the angular frequency, $g = 274$ m s^{-2} is the gravitational acceleration at the Sun's surface, and $k = l/R_\odot$ is the horizontal spatial wavenumber expressed in terms of the spherical harmonic degree l and the solar radius $R_\odot$. High-degree f modes propagate horizontally. MDI full-disk data show that f modes are excited with a similar frequency envelope to the acoustic p modes, peaking near circular frequency $\nu = \omega/2\pi = 3$ mHz with a full width at half maximum of 1 mHz. The envelope peak occurs near $l = 880$ and the full power width covers the degree range 600-1200. In this range the f mode kinetic energy is concentrated within 2 Mm of the solar photosphere.

There are several advantages to using the f mode as a tracer of flows near the solar surface. Using the time-distance technique, there is direct sensitivity to both horizontal components of the flow. Already this is much better than direct Doppler measurements, which see only the line-of-sight component. In this respect the f-mode time-distance technique is similar to correlation tracking of granulation (DeRosa et al., 2000). Other techniques for measuring vector flows include ring diagrams (Hill, 1988), p-mode time-distance helioseismology (Duvall et al., 1996) and knife-edge diagnostics (Lindsey et al., 1996). With f modes, there is no direct sensitivity to vertical motion, although by examining the horizontal divergence it may be possible to estimate the vertical motion. Because we know the f-mode eigenfunctions, the depth over which we are averaging is well defined (Fig. 2.1a).

As f modes have not been been used in time-distance helioseismology before, the purpose of this section is to test the utility of the technique by first observing well-known phenomena. To this end, we simultaneously measure three tracers of solar rotation that in the past have given similar yet consistently different rotation rates (Beck, 2000). By using the same instrument with simultaneous observations, we expect that some of the possible systematic errors will be common. The first tracer we use is the f-mode advection rate determined from time-distance helioseismology, which we identify as a proxy of the surface rotation. This is compared to the surface Doppler rate averaged over 18 years by Snodgrass & Ulrich (1990). The tracer that gives the highest apparent rotation rates is the supergranulation pattern (Duvall, 1980; Snodgrass & Ulrich, 1990). The third tracer is obtained by tracking the small magnetic features (Komm et al., 1993b).

2.1.2 Observations

MDI full-disk Dopplergrams (Scherrer et al., 1995) were used to study flows for the time period 1999 April 14, 16h UT to 1999 April 20, 16h UT, or a total of six days. The region studied was centered at Carrington longitude 180°. This particular region was picked because it was quiet and the data coverage was very good as it was during MDI's three months of continuous coverage for 1999 (97.3% of the minutes had usable data during the six days). Three separate regions were studied, with all three of size 45° in longitude and in latitude, with one centered on the equator, one centered at 40° North and the other at 40° South. There is some overlap between the regions, and as the equatorial and higher latitude areas were tracked at different rotation rates, this difference was used to calibrate one of the signals, as described below. The B_0 angle was $-5°$ during the observations, and we estimate that latitudes ranging from $-55°$ to $+45°$ can be analyzed safely.

Doppler images were calibrated and located in the CCD frame using the normal MDI pipeline routines. The first step in the analysis is the tracking of the regions to be studied. Images were interpolated onto Postel's azimuthal equidistant projection (Pearson, 1990) centered on a point in latitude 0°, +40°, $-40°$ and at longitude

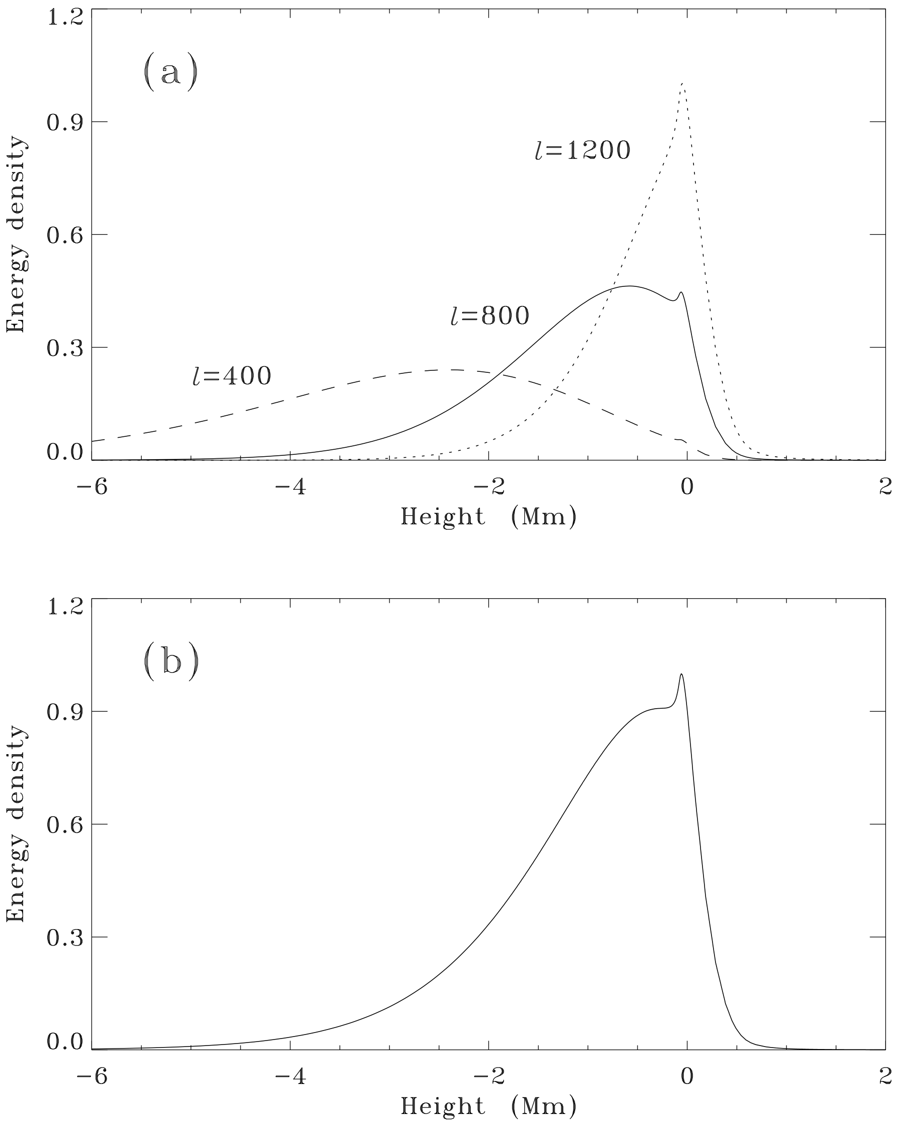

Figure 2.1: F-mode kinetic energy density versus height z, defined by $\rho(z)e^{2kz}$ where ρ is the density and k the wavenumber. **(a)** Kinetic energy density for f modes with degrees 400, 800 and 1200. Calculations are for a plane-parallel atmosphere with constant gravity. The height is measured from the photosphere (radius 695.99 Mm). A free surface is placed 2 Mm above the photosphere. The internal density is taken from the standard solar model of Christensen-Dalsgaard et al. (1993). Above the temperature minimum, density is from the chromospheric model C of Vernazza et al. (1981). Curves are normalized to the same arbitrary constant. **(b)** Average kinetic energy density versus height for the f modes used in this study. The mean and standard deviation of this distribution are respectively -1.05 Mm and 1.01 Mm. The location of the absolute maximum coincides with the highly superadiabatic layer.

180°. The azimuthal equidistant projection is linear in great-circle distance measured from the central point of the projection to outlying points. This projection is used rather than a longitude-sin(latitude) projection so that three-dimensional Fourier filtering can be used on the data more effectively. The regions were followed at a rate appropriate for the central latitude and consistent with the supergranule pattern rate measured by Snodgrass & Ulrich (1990). During the time period of the observations MDI was observing both full-disk Dopplergrams and magnetograms with one-minute cadence. Both Dopplergrams and magnetograms were processed by the above procedure so that detailed comparisons between the two could be made. A smooth background image (spatial scale 0.2 $R_{\odot}$) was subtracted from each Dopplergram before the projection.

The magnetograms were also processed to remove cosmic rays and smoothed in time. To remove the effect of cosmic rays striking the CCD during the exposure/readout, the temporal pixel-by-pixel median of three successive images was taken and the resultant median replaced the middle image. The cosmic rays commonly affect pixels in a small neighborhood but only for a single image and so are generally removed by the median procedure. This procedure also smooths the field on a three-minute time scale. After the median procedure, images over a ten-minute interval are averaged and a new time series is constructed of these ten-minute means.

To obtain travel times, a similar procedure is used as for p modes (Duvall et al., 1997), except that the filtering is a little different. For each 8-hour interval, the datacube goes through a three-dimensional Fourier filter that cuts off power below 2 mHz (mostly supergranulation) and isolates the f mode ridge. The resultant power spectrum peaks near $\nu = 2.9$ mHz and spherical harmonic degree $l = 800$. The full widths at half maximum are $\Delta\nu = 0.7$ mHz and $\Delta l = 400$. Figure 2.1b displays the average kinetic energy density versus depth for the average wave packet. We see that we can probe the first 2 Mm below the solar surface, with maximum sensitivity at a depth of 1 Mm.

The temporal signal at a central pixel is cross-correlated with the signals in the four quadrants of an annulus centered in arc distance, as described in chapter 1. These quadrants are centered on the cardinal directions north, south, east, and west. Before measuring the travel times, average cross correlations are made for the waves propagating in the directions west-east and north-south. Additional averages are made for waves propagating outward from the center and inward toward the center of an annulus. The difference between outward and inward travel times is expected to be proportional to the horizontal divergence of the flow. In addition, to make the signal-to-noise acceptable, the cross correlations for a 2×2 grid of origins are averaged, thereby reducing the spatial resolution of the resultant maps by a factor of two below that of the original data.

The thickness of an individual annulus is the same as the spatial sampling of the original images, or 0.12° . Four of these are combined during the fitting process, and so all pixels from 0.42° to 0.9° are used in the measurements. The angle 0.9° corresponds to a distance of 7.5 pixels in the original spatial sampling and 3.75 in the reduced spatial scale.

The cross correlations were then fit by least squares to a harmonic function multiplied by a gaussian envelope, sometimes called a Gabor wavelet. This functional form has been used for the case of p modes (Kosovichev & Duvall, 1997), and seems to work reasonably well for the f modes. The difference between phase times for counter-propagating waves is proportional to the local horizontal flow velocity (Kosovichev & Duvall, 1997).

2.1.3 Supergranulation Pattern

Supergranulation on the surface of the Sun is a pattern of horizontal outflows with a distinct scale of 30 Mm and an apparent lifetime of 1 day, outlined by a network of small magnetic features. An example of the divergence signal (inward minus outward travel time) for one of the 18 8-hour intervals analyzed is shown in Fig. 2.2 with magnetic field information overlaid. A white, or positive signal, corresponds to an outflow from the center. From the size of the features present, their lifetime, and the presence of the magnetic field in the dark lanes, we identify supergranulation as the main contributor to the signal. This can also be seen by making a spatial power spectrum of the 18 frames covering the 6 days. Averaging over all temporal frequencies, the spatial spectrum is shown in Fig. 2.3. The peak near degree $l = 120$ is characteristic of the supergranulation and has been seen before in the surface Doppler observations (e.g. Hathaway et al., 2000). The histogram of the divergence

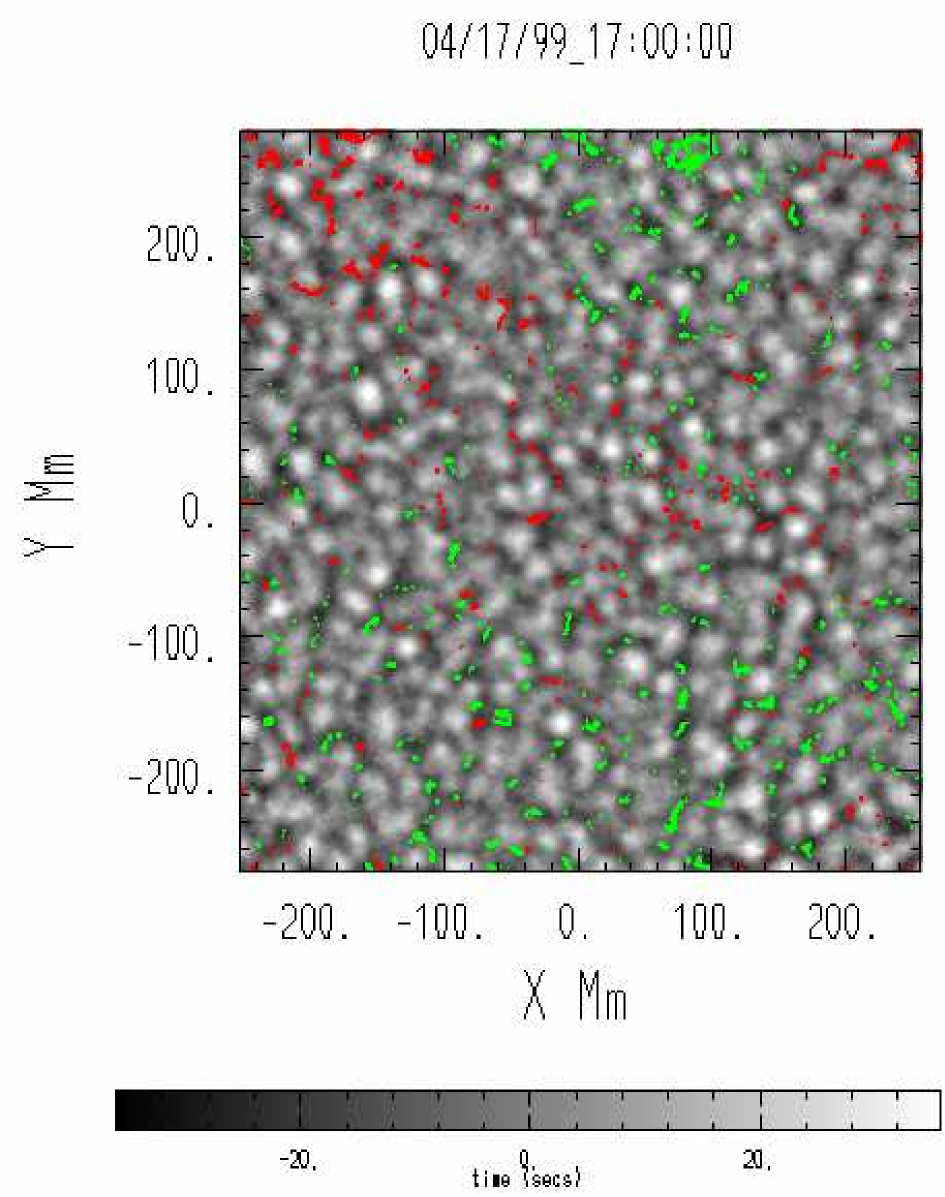

Figure 2.2: Example of the divergence signal (inward travel times minus outward times) with small magnetic features overlaid. Magnetic field is displayed as green and red for the two polarities when the magnitude of the field is larger than 15 Gauss. The gray scale is for the divergence signal with white shades for outflow and dark shades for inflow. The color-bar indicates the travel time difference in seconds. The line Y=0 corresponds to the equator and X=0 corresponds to Carrington longitude 180°. The time-distance data is averaged over 8.5 hours starting at the time shown on top.

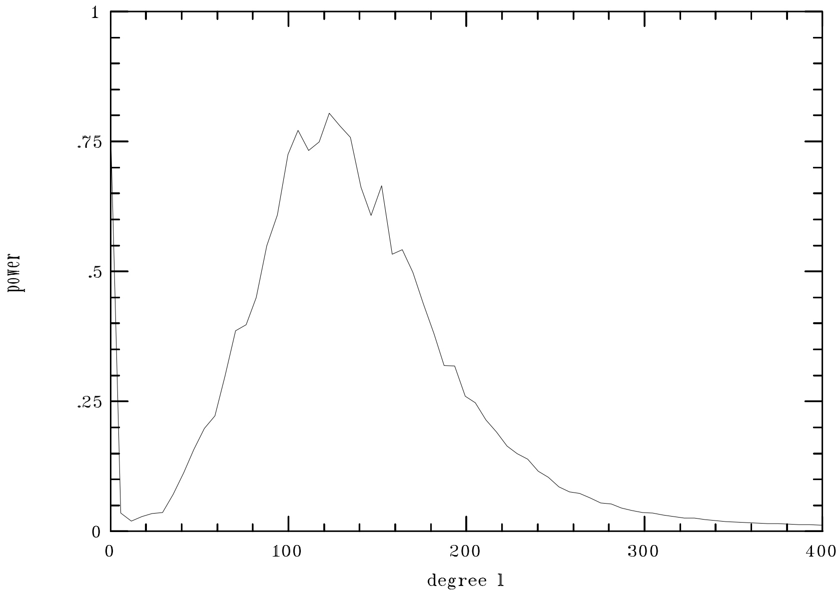

Figure 2.3: Power versus horizontal wavenumber averaged over temporal frequency and azimuth for the divergence signal (inward travel times minus outward times). The power scale is arbitrary.

signal is shown in Fig. 2.4. An asymmetry between the regions of divergent and convergent flows is clearly seen. There are more points associated with a convergent flow than with a divergent one, and the distribution is skewed. It should be noted that both these properties are present in simple models of incompressible hexagonal convection near onset (e.g. Veronis, 1959).

In Fig. 2.5 we show the temporal power spectrum of the divergence signal averaged over all spatial frequencies. We see that much of the power is at very low frequencies, with 85% of the power below 6 μHz. This is reasonably consistent with a Lorentzian-shaped temporal spectrum, as suggested in the Harvey (1985) model, although we note that the power peaks at a non-zero frequency. We also studied the temporal correlation of these images and found that it was significantly negative (-0.1) at a time lag of 3 days, consistent with the observation that new supergranules appear near the boundaries of old supergranules (Shine et al., 2000).

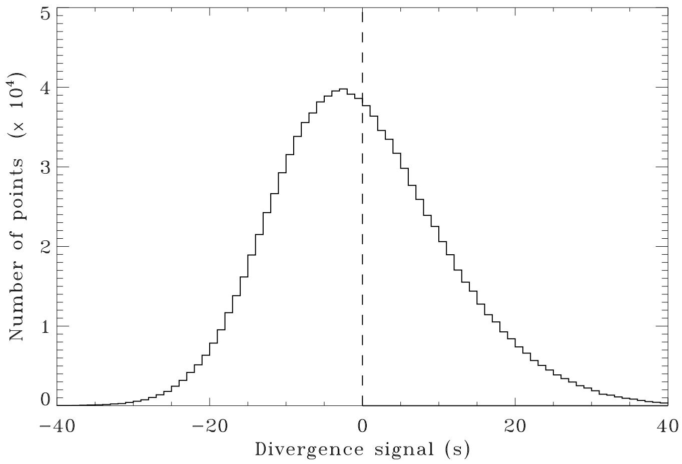

Figure 2.4: Histogram of the divergence signal (inward travel times minus outward times). The maximum of the histogram occurs near −2.5 s and the skewness is 0.42. There are about 20% more points with negative divergence than positive divergence.

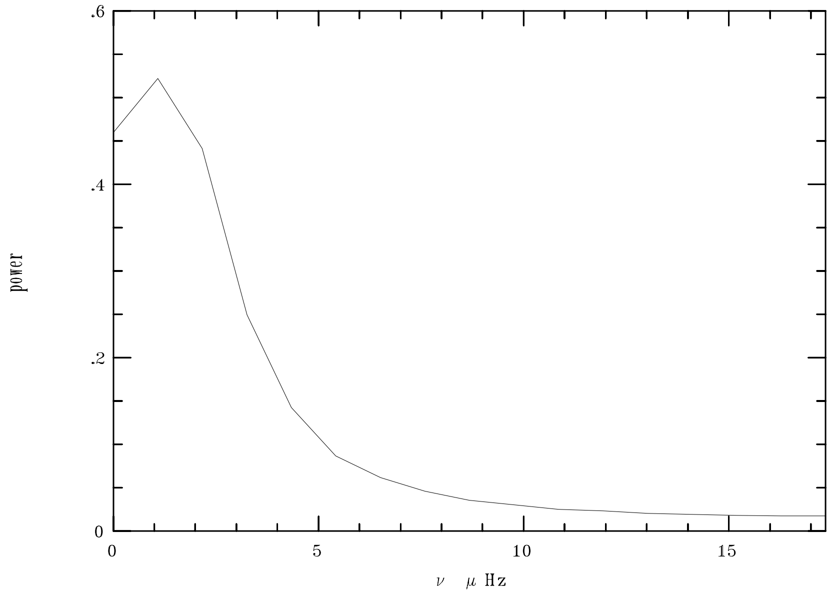

Figure 2.5: Power of the divergence signal versus temporal frequency averaged over horizontal wavenumber. The power scale is arbitrary.

2.1.4 Rotation and Meridional Circulation

To measure differential rotation, we take the difference between the eastward and the westward travel times, $\delta\tau^{\rm ew}$. After averaging in longitude, we obtain $\delta\tau^{\rm ew}(\lambda)$ versus latitude, λ. In order to convert the travel-time difference into a westward velocity, v_x, we seek a calibration constant α such that

$$v_x(\lambda) = \alpha \, \delta\tau^{\rm ew}(\lambda) \; . \tag{2.1}$$

Because the three regions centered at latitude $-40°$, $0°$, and $40°$ were tracked at different known tracking rates and because they overlap in latitude (each is $90°$ wide), it is possible to derive α from the data. We require that the velocity be the same for the equatorial region (eq) and for the northern region (up) where they overlap:

$$V(0°) + \alpha \;\; \delta\tau^{\rm ew}(\lambda)\big|_{\rm eq} \equiv V(40°) + \alpha \;\; \delta\tau^{\rm ew}(\lambda)\big|_{\rm up} \qquad \text{for} \quad 35° < \lambda < 45° \; , \tag{2.2}$$

where $V(\lambda)$ is the differential rotation velocity from Snodgrass & Ulrich (1990). The optimal calibration constant is $\alpha = 7.08$ m s^{-2}. The angular velocity is then given by $\Omega = (v_x + V)/(R_\odot \cos\lambda)$. As a check, we then compare the angular velocity in the overlap region between the equatorial and southern regions and find excellent agreement within 0.3 nHz.

The angular velocity Ω from f modes is compared with the long-term average of the surface Doppler rate in Fig. 2.6a. We see that the two agree rather well. We also measured the near-surface meridional circulation from the south-north travel-time differences using the calibration constant α. The results are shown in Fig. 2.6b, compared with the motion of the magnetic features measured by Meunier (1999). It appears that from six days of data we can make remarkably consistent measurements of rotation and meridional circulation.

To study rotation of the supergranulation pattern we tracked the divergence signal in time, with a time-lag of 8 hour. At each latitude, one-dimensional spatial cross-correlations were computed. The cross-correlations are averaged and then fit to a Gaussian function. The spatial shift at correlation maximum is converted to a longitude, divided by eight hours, and added to the tracking rate to determine

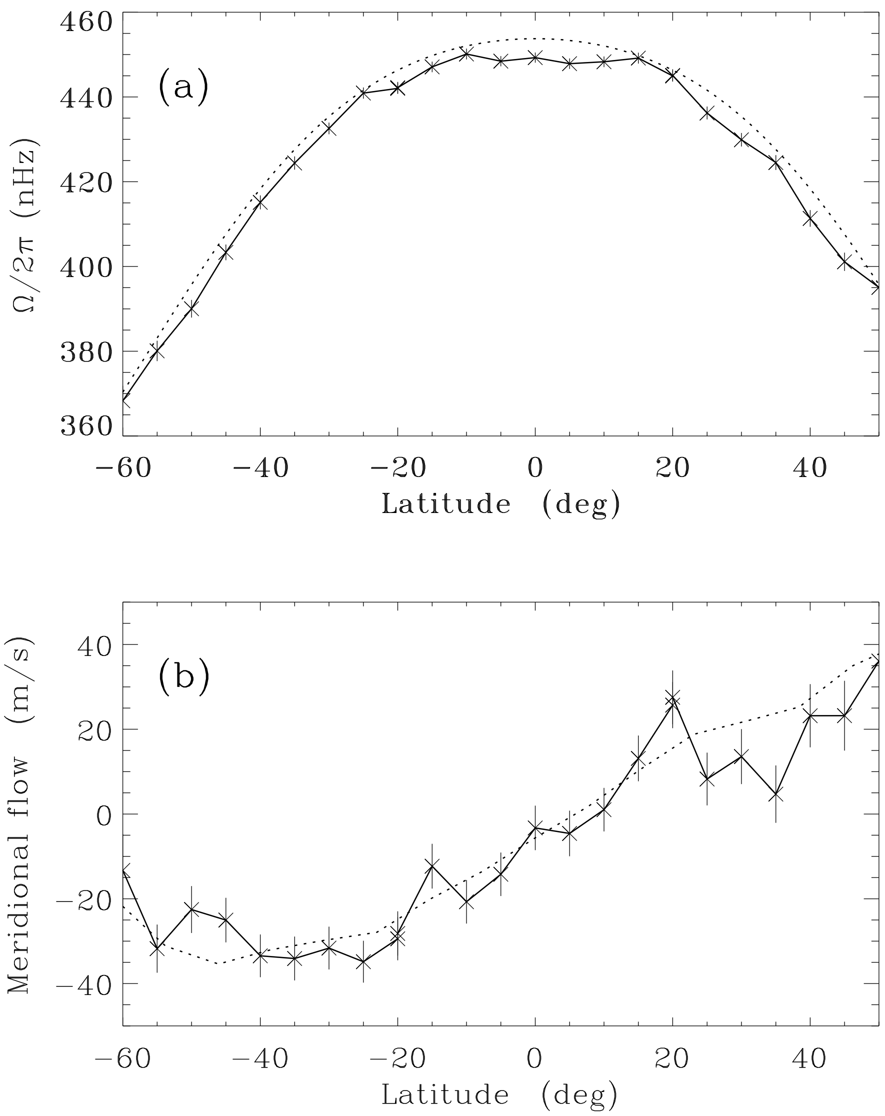

Figure 2.6: (a) f-mode advection rotation rate (solid curve) and surface Doppler rotation (dashed curve) versus latitude. The surface Doppler rate is the average from 1967-84 given by Snodgrass & Ulrich (1990), which is found to be 3.4 nHz higher on average. (b) Meridional circulation versus latitude. The solid curve and crosses are the f-mode measurements. The dashed curve is from the motion of the small magnetic features (Meunier, 1999) for the first year of MDI operation in 1996-97.

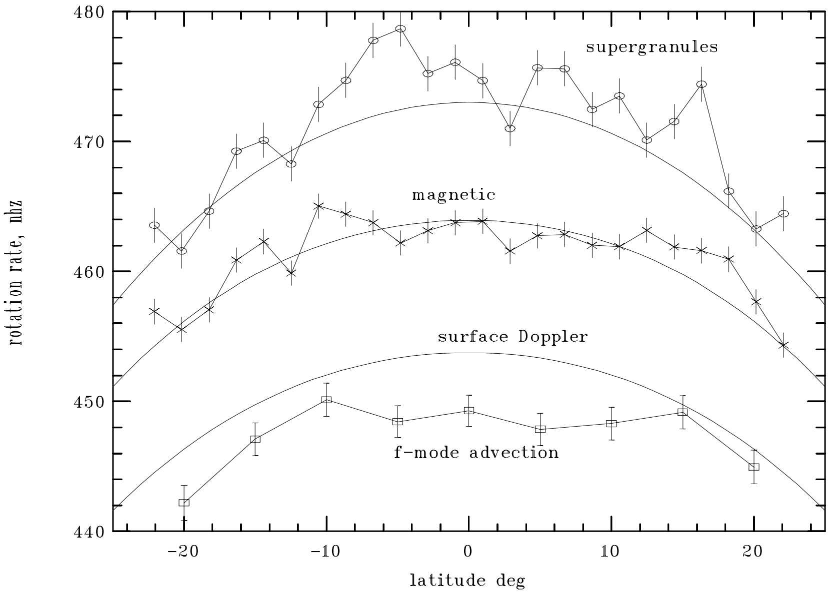

Figure 2.7: Rotation rates measured in this work compared with previous works. From the top, the open circles with error bars are derived from the supergranulation patterns of the divergence signal (this work) and the solid line through the values is the supergranulation feature rate for years 1967-1987 of Snodgrass & Ulrich (1990). In the middle, the crosses with error bars are from the MDI magnetic correlations (this work) and the underlying solid line plots the average over years 1975-1991 of the small magnetic feature rate (Komm et al., 1993b). At the bottom, the open squares with error bars are the f-mode advection measurements from this study and the nearby solid line is from the average surface Doppler rotation rate for years 1967-1984 of Snodgrass & Ulrich (1990).

a pattern rotation rate. The procedure for the small magnetic features is similar except that the time-lag is ten minutes, as this gave the smallest errors.

The three rotation measures are compared with previous work in Fig. 2.7. We find that there is good agreement with earlier data averaged over decades. This figure confirms differences between the rotation rate of the plasma near the solar surface and the apparent rotation rates of supergranulation and magnetic features. It was suggested long ago (Foukal, 1972) that the difference between the rotation of magnetic patterns and the surface Doppler rate may be due to magnetic structures being “rooted” in deeper, more rapidly rotating layers. The high supergranulation rate is more puzzling. An explanation is presented in the next section.

To learn more about the difference between the rotation rates of the supergranulation pattern and the small magnetic features, we examined a movie made from frames similar to Fig. 2.2. After removing differential rotation, the movie confirmed that a small motion of the magnetic features can be seen in the eastward direction (slower rotation) with respect to the supergranulation network. The magnetic features stayed in the dark lanes (convergent flows) as this slow apparent drift took place.

Simultaneous measurements of velocity and magnetic field with MDI is a powerful combination to study the dynamics of the near solar surface. Time-distance helioseismology of the f mode has been shown to be a useful tool to study horizontal flows. In the next section, we focus on the mysterious dynamics of the supergranulation using the same time-distance technique but a much longer MDI data set.

2.2 The Dynamics of Supergranulation

The dynamics of the supergranulation is poorly understood and there is as yet no explanation for the observation that the supergranular pattern appears to rotate faster than the magnetic features. In this section we show that supergranulation undergoes oscillations and supports waves with periods of 6-9 days. The nature of supergranulation appears to be travelling-wave convection. The waves are predominantly prograde, which explains the apparent superrotation of the pattern.

2.2.1 Introduction

Convective-like motion on the solar surface consists of two main components: granulation and supergranulation. Granules, with a typical size of 1.5 Mm, are well understood as a convective phenomenon and can be studied with realistic numerical simulations (Stein & Nordlund, 2000). Supergranules, however, have remained puzzling since the early observations by Hart (1954). Hart (1956) described local variations with a spatial periodicity of 26 Mm and an rms velocity of 0.3 $\mathrm{km\,s^{-1}}$, but rejected a convective instability as an explanation on the basis that the scale of the phenomenon was too "large". In a classic paper, Leighton et al. (1962) reported "large cells of horizontally moving material distributed roughly uniformly over the entire solar surface" that are outlined by the chromospheric network. It is worth citing the physical description of supergranulation given by Simon & Leighton (1964) nearly forty years ago, as it summarizes the current paradigm:

"*The observed cellular flow pattern of the large-scale motions is strongly suggestive of convective motions, and we tentatively propose that we are dealing with a larger scale version of the familiar photospheric granulation – a supergranulation. The observed dimensions of the large cells (32000 km) suggest that they originate in the Sun's convective envelope which extends from the bottom of the photosphere to depths of 5000-100000 km. Although the lifetime (20 h) of the supergranulation appears very long at first glance, if one considers the small velocity and the large dimensions one finds that the matter in all probability does not circulate more than once. This fact, coupled with the very irregular size and shape structure of the cells, suggests that we are observing an example of non-stationary convection, rather than* *the stationary laminar convection of classical Bénard cells. Since we are able to observe the supergranulation only from above, we have no means of determining the geometrical shape of the convection pattern; it may be either a circulating flow or a columnar convection such as a cloud or plume... In view of these considerations it seems proper to ask whether there is a possible mechanism in the Sun which would select cell depths of roughly 5000 km. A possible answer lies in the ionization zones of either neutral He atoms or singly ionized He^+, or perhaps both."*

"The observed horizontal motions provide a mechanism for building up relatively strong fields in a narrow network pattern, as is observed. These magnetic channels in turn suggest an explanation for the origin of the Ca^+ emission network... Magnetic fields would tend to be swept to the cell boundaries by the horizontal currents, and concentrate there in strengths several times greater than the average field. "

This description makes a lot of sense, although some points still need confirmation. Despite several studies (e.g. Simon & Weiss, 1968) it remains to be shown that a convective instability due to the recombination of ionized Helium is the origin of the distinct supergranular scale. The depth of the supergranulation layer is largely unknown. It has been suggested that the properties of convective motions in a highly stratified atmosphere may imply that supergranules are a deep phenomenon, with depths in excess of their horizontal diameters (Parker, 1973). Local helioseismic studies show that the correlation between internal flows and surface flows appears to switch sign at depths of 5-10 Mm (Duvall, 1998; Zhao, 2003; Braun & Lindsey, 2003), suggesting the existence of a "return flow" below these depths. There have been a number of studies related to the influence of supergranular flows on magnetic fields. It has been shown that a stationary cellular flow tends to expel the magnetic field from the regions of fluid motion and concentrate the flux into ropes at the cell boundaries (Parker, 1963; Galloway et al., 1977; Galloway & Weiss, 1981). For obvious reasons of simplicity, analytical or semi-analytical studies often picture supergranulation as laminar convection, although, as noted above by Simon & Leighton (1964), the flows must be highly turbulent and non-stationary. Recent numerical simulations of stratified convection at high Rayleigh number have revealed a very complex picture. It is now accepted that heat and momentum transport in solar-like turbulent convection is controlled by a network of coherent cyclonic plumes sinking from the thermal boundary layer (Julien et al., 1996; Brummell et al., 1996). The dynamics of individual plumes is dominated by strong vortex-vortex interactions with neighboring plumes (Julien et al., 1996). Rast (2003) claims that the scale of supergranulation may have its origin in the interaction and merging of individual granular plumes (see also Ploner et al., 2000). A somewhat related model was proposed earlier by Rieutord et al. (2000, 2001) whereby supergranulation is the result of a nonlinear large-scale instability of the granular flow, triggered by exploding granules. In both these models, supergranulation is not a proper scale of thermal convection, and the depth of supergranulation is determined by the depth at which network plumes can remain stable (Rast, 1997). Realistic numerical simulations will be crucial in understanding the nature of supergranulation. Yet, the solar convection zone is so highly turbulent and stratified that numerical modeling at supergranular scales has remained elusive.

On the observational side, the original work of Leighton and coworkers has been refined. A variety of methods have been used to characterize the distribution of the cell sizes. A characteristic scale can be obtained from the spatial autocorrelation function (e.g. Hart, 1956; Simon & Leighton, 1964; Duvall, 1980), the spatial Fourier spectrum (e.g. Hathaway, 1992; Beck, 1997), and segmentation or tessellation algorithms (Hagenaar et al., 1997). Although definitions vary, average cell sizes are in the range 15-30 Mm. The topological properties of the pattern have been studied by Schrijver et al. (1997). It is unclear whether there is a variation of cell sizes with latitude: Rimmele & Schroeter (1989) and Komm et al. (1993a) report a possible decrease with latitude, Berrilli et al. (1999) an increase, and Beck (1997) no significant variation. The typical "lifetime" of the supergranular/chromospheric network, obtained by fitting an exponential decay to the correlation function, is found to be about 1 day (e.g Rogers, 1970; Worden & Simon, 1976; Duvall, 1980; Wang & Zirin, 1989). An important observation by Beck & Duvall (2001) shows that the temporal autocorrelation of the supergranulation pattern does not follow a simple exponential decay with time but becomes negative after a few days. Thus e-folding lifetimes may be misleading (we will come back to this point later). The typical rms horizontal velocity of supergranular flows is known to be about 0.3 $\mathrm{km\,s^{-1}}$(e.g. Hathaway et al., 2000). However, the vertical component of the flows has been extremely difficult to measure (e.g. Giovanelli, 1980) or infer (November, 1989). Miller et al. (1984) cautioned that Doppler velocity measurements at the cell boundaries may be polluted by the network field. The best estimate is perhaps due to Hathaway et al. (2002) who find that the vertical flows have speeds of about 10% of their associated horizontal flows or about 30 $\mathrm{m\,s^{-1}}$, although the topology of the vertical flows is largely unknown. Perhaps even more difficult to measure are the related temperature fluctuations. Observers have searched for the thermal signature of a convective process, i.e. rising hot material at the cell centers and sinking cool material at the cell boundaries. Unfortunately, answers vary too widely (see Lin & Kuhn, 1992, and references therein).

2.2.2 Anomalous Motion of the Pattern

Duvall (1980) showed that the rotation of the supergranular pattern is faster than the photospheric plasma by approximately 5%. This anomaly has since been confirmed by Snodgrass & Ulrich (1990) who used a local correlation tracking method with a time-lag of $\Delta t = 24$ hr (see Fig. 2.7). In order to study this point in more detail, we constructed a series of f-mode divergence maps of size $90° \times 90°$ for the whole 1996 dynamics period (2 months) following the same method as described in the previous section. To quantify the apparent motion of supergranules in the divergence maps we used a local correlation tracking method (e.g. DeRosa, 2001) with various time-lags Δt between frames. Around each point, we consider a small region apodized by a Gaussian surface with a full width at half maximum of 3.84°, i.e. about twice the supergranulation scale (see Fig. 2.8). At fixed Carrington longitude, small regions separated by Δt are spatially cross-correlated. The spatial displacement at correlation maximum, $\Delta \boldsymbol{x}$, is obtained by fitting a parametric surface to the cross-correlation. Three different parametric models were used for the fits (product of Gaussian functions, cylindrical Bessel function $J_1(r)/r$, product of sinc functions). On average, we did not find a significant model-dependent bias. The accuracy of the feature tracking algorithm was successfully tested on divergence maps locally shifted by known amounts. The apparent velocity of the pattern is then given by $\boldsymbol{u}_{\mathrm{LCT}} = \Delta \boldsymbol{x}/\Delta t$.

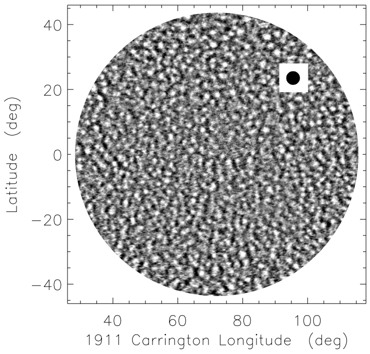

Figure 2.8: An individual map (8 hr average, 1996 MDI Dynamics run) of the horizontal divergence of the flow field. White shades indicate a positive divergence. Around each point, we consider a small region apodized by a Gaussian surface with a full width at half maximum of 3.84° (black disk). Small regions separated by a time-lag Δt are spatially cross-correlated. The spatial displacement at correlation maximum, $\Delta \boldsymbol{x}$, corresponds to the apparent velocity $\boldsymbol{u}_{\mathrm{LCT}} = \Delta \boldsymbol{x}/\Delta t$.

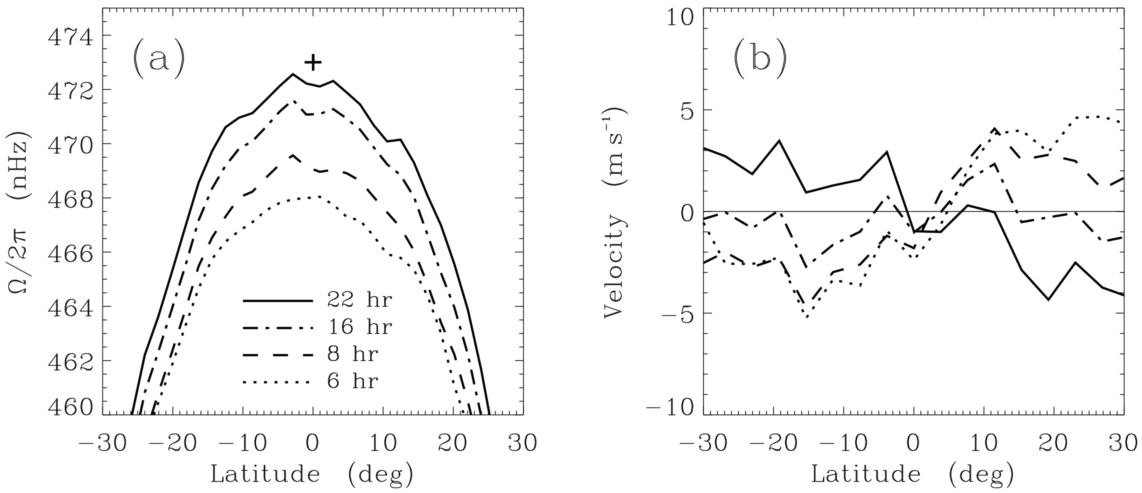

Figure 2.9: Anomalous flows derived from the temporal evolution of the supergranulation pattern, using a local correlation tracking method. **(a)** Apparent rotation of the supergranulation pattern for $\Delta t = 6$, 8, 16, and 22 hr. For comparison, the cross shows the equatorial rotation obtained by Snodgrass & Ulrich (1990) for $\Delta t = 24$ hr. **(b)** Apparent meridional circulation as a function of time-lag, Δt. The meridional motion appears to be equatorward for $\Delta t > 20$ hr. A P-angle correction was applied to the data.

Figure 2.9 shows the apparent rotation and meridional circulation that we obtained as a function of Δt. The meridional circulation is very small and even equatorward for large Δt. The rotation rate increases rapidly with Δt. It has been speculated (e.g. Corbard & Thompson, 2002) that the fast rotation of the pattern may be a consequence of convective cells deeply rooted in the shear layer below the surface (rotation increases inward at low latitudes). However, Beck & Schou (2000) point out that rotation measured from correlation tracking ($\Delta t = 24$ hr) is faster than the rotation of the solar plasma measured at *any* depth in the interior. It is especialy puzzling that the rotation of the magnetic network (Komm et al., 1993b) is also less than that of the supergranular pattern, since magnetic fields are expected to be strongly advected by supergranular flows. To date, a definitive explanation of the excess rotation speed of the supergranular pattern has not been presented.

In the following, we study yet another time series of flow maps of the solar supergranulation, obtained from f-mode time-distance helioseismology. These data of even larger size ($120° \times 120°$) cover the whole 1996 Dynamics run and enable us to characterize, for the first time, the true dynamics of the supergranulation. We find that the power spectrum appears to be consistent with a spectrum of traveling waves (Gizon et al., 2003).

2.2.3 Supergranulation Supports Waves

Turbulent solar convection is commonly characterized by an autocorrelation function that exhibits an exponential decay in time (Harvey, 1985; Kuhn et al., 2000), leading to a power spectrum that is a decreasing function of temporal frequency. That supergranulation may not follow such a simple model has been hinted at previously. For example, the observed autocorrelation function becomes negative after 60 hr (Beck & Duvall, 2001) and new supergranular cells appear to form near the boundaries of decaying cells (Shine et al., 2000). The negative excursion of the autocorrelation function leads to a power spectrum peaked at a low non-zero frequency (Duvall & Gizon, 2000, and previous section), suggesting an underlying long-range order.

To study supergranulation, we use a 60-day sequence of Doppler velocity images obtained in 1996 by the Michelson Doppler Imager (Scherrer et al., 1995) on board

SOHO. MDI full-disk Dopplergrams are observed at a one-minute cadence with a spatial sampling of 0.12° at disk center. Images are tracked at the Carrington angular velocity ($\Omega_{\rm C} = 2.87$ μrad s^{-1}) to remove the main component of solar rotation. We apply the techniques of time-distance helioseismology (Duvall et al., 1993b) to obtain every 12 hr a $120° \times 120°$ map of the horizontal divergence of the flows in a 1 Mm-deep layer beneath the surface (Duvall & Gizon, 2000). Unlike raw Doppler images, the divergence signal has uniform sensitivity across the solar disk and is subject to few systematic errors. Supergranules appear as cellular patterns of horizontal outward flow in the divergence maps.

The divergence maps are obtained by measuring the time it takes for solar f modes to propagate from any given point on the solar surface to a concentric annulus around that point. The difference in travel times between inward and outward propagating waves is a proxy for the local horizontal divergence of the flow field. Images were interpolated onto Postel's azimuthal equidistant projection (Pearson, 1990) centered on latitude 0° and Carrington longitude at image center. Data cubes go through a three-dimensional Fourier filter to isolate the f-mode ridge and cut off the power below 2 mHz (supergranulation noise). The temporal signal at a given pixel is cross-correlated with the signal in a concentric annulus of thickness 0.12°. The cross-correlation function contains information about waves propagating outward and inward from the central pixel depending on the sign of the correlation time lag. To enhance the signal, cross-correlations are averaged on a 2×2 grid of origins, corresponding to a spatial sampling of 0.24° at image center. Travel times for inward and outward propagating waves are measured by fitting a Gaussian wavelet to the cross-correlations. Travel-time differences are then averaged for a range of annuli (mean radius 15 Mm). The divergence maps are finally interpolated onto a Carrington longitude-latitude grid with a resolution of 0.24° in both coordinates.

For any given target latitude, λ, we extract a longitudinal section of the data 10° wide in latitude centered about λ. The divergence signal is Fourier transformed in three dimensions to make power spectra as a function of frequency, ν, and horizontal wavevector, $\boldsymbol{k} = (k_x, k_y)$, where k_x and k_y are in the East-West and South-North directions respectively. In cylindrical coordinates, $\boldsymbol{k}$ is uniquely specified by its

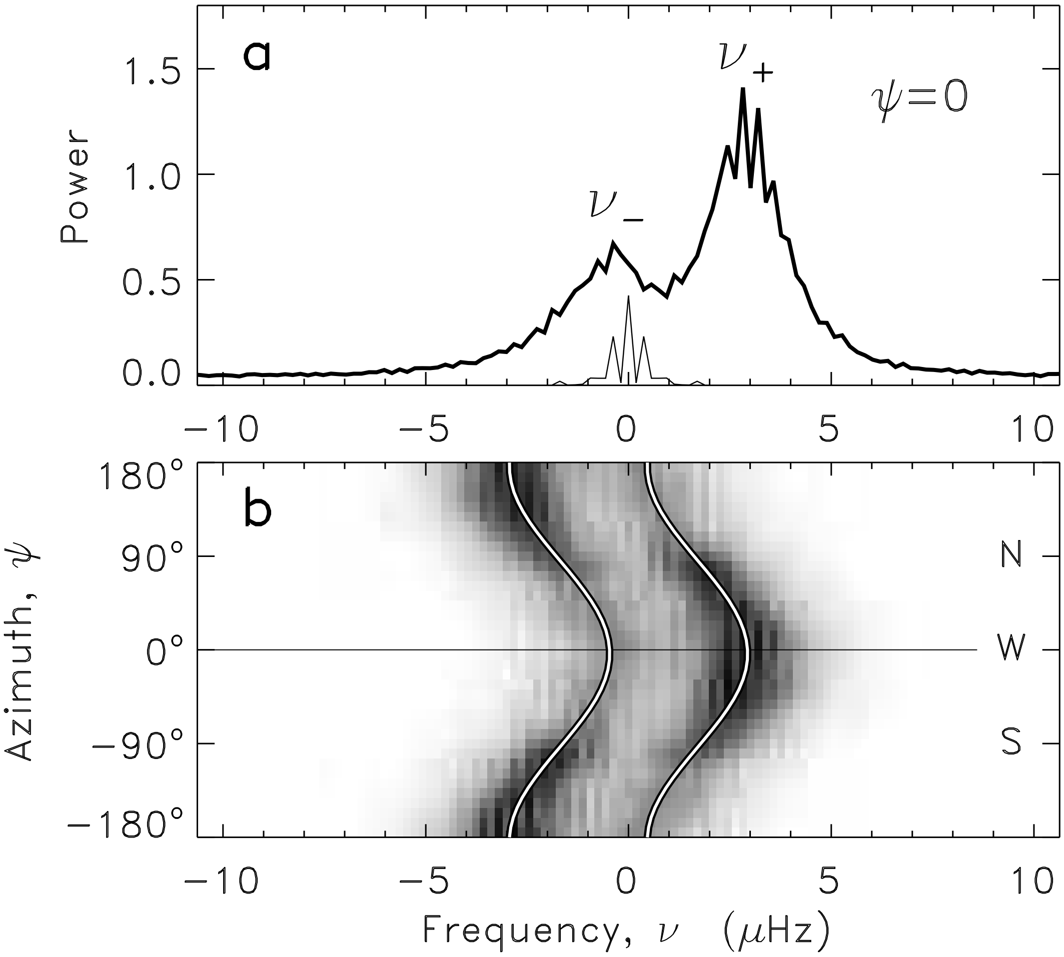

Figure 2.10: Power spectrum of the supergranulation signal near the equator ($\lambda = 0°$). Cuts are shown at constant wavenumber $k = 120/R$ where R is the solar radius. **(a)** The thick line is the power spectrum versus frequency, ν, for $\boldsymbol{k} = (k, 0)$ pointing in the direction of solar rotation, $\psi = 0$ (West). There are two peaks at frequencies ν_- and ν_+. The frequency resolution is given by the power spectrum of the temporal window function (thin line). **(b)** Cylindrical cut, $P_k(\nu, \psi)$, in the power spectrum at constant k versus ν and the direction of $\boldsymbol{k}$, ψ. By construction, $P_k(\nu, \psi) = P_k(-\nu, \psi - \pi)$. Power peaks in two ridges at frequencies $\nu_-(\psi)$ and $\nu_+(\psi)$. For each ψ, we measure $\nu_\pm$ by fitting the sum of two independent Lorentzian functions to the power. The fits take into account the convolution by the window function. The sinusoidal variation of $\nu_\pm$ with ψ is due to advection by a background flow $\boldsymbol{u} = (u_x, u_y)$. The double lines show the fit $\nu = \pm\nu_0 + (ku_x \cos\psi + ku_y \sin\psi)/2\pi$ to $\nu_\pm(\psi)$, where ν_0 is a constant frequency. At the equator we find $\boldsymbol{u} = (43, 0)\ \mathrm{m\,s^{-1}}$. The velocity u_x is measured in a frame co-rotating with the Sun at the Carrington rotation rate. (Gizon et al., 2003)

magnitude, k, and its direction, ψ, such that

$$k_x = k\cos\psi \tag{2.3}$$

$$k_y = k\sin\psi\ . \tag{2.4}$$

Figure 2.10 shows cuts in the equatorial power spectrum at a constant k typical of the supergranulation. For each azimuth ψ, the power has two broad peaks at frequencies ν_+ and ν_- (Fig. 2.10a). No Galilean transformation can cause these peaks to coalesce, at zero frequency or otherwise. This implies that the supergranulation undergoes oscillations.

For each azimuth, we measure the frequencies ν_+ and ν_- by fitting the sum of two Lorentzian functions to the power (Fig. 2.10b). Observations show that the difference $\nu_+ - \nu_-$ is essentially independent of azimuth, and $\nu_\pm$ have a sinusoidal dependence with ψ of the form:

$$\nu_\pm = \pm\nu_0 + \nu_1\cos(\psi - \psi_0)\ . \tag{2.5}$$

We interpret ν_1 to be a Doppler frequency shift,

$$\nu_1 = k\|\boldsymbol{u}\|/2\pi\ , \tag{2.6}$$

produced by a horizontal background flow $\boldsymbol{u}$ pointing in the direction ψ_0, as one does in helioseismological ring analysis (Schou & Bogart, 1998). The nearly linear relationship measured between ν_1 and k in the range $40 < l < 180$ ($l = kR_\odot$) is consistent with this interpretation. The latitudinal dependence of $\boldsymbol{u}$ is shown in Figure 2.11. The inferred rotation (Fig. 2.11a) and meridional circulation (Fig. 2.11b) are both remarkably similar to that of the small magnetic features (Komm et al., 1993b,c). This property is consistent with the view that magnetic fields are advected by supergranular flows.

The dynamics of the supergranulation are best studied once the background flow, $\boldsymbol{u}$, has been removed. In a co-moving frame, each spatial component oscillates at a characteristic frequency ν_0. We find a clear relationship between ν_0 and the wavenumber k, well described by a power law (Fig. 2.12a). This is a fundamental

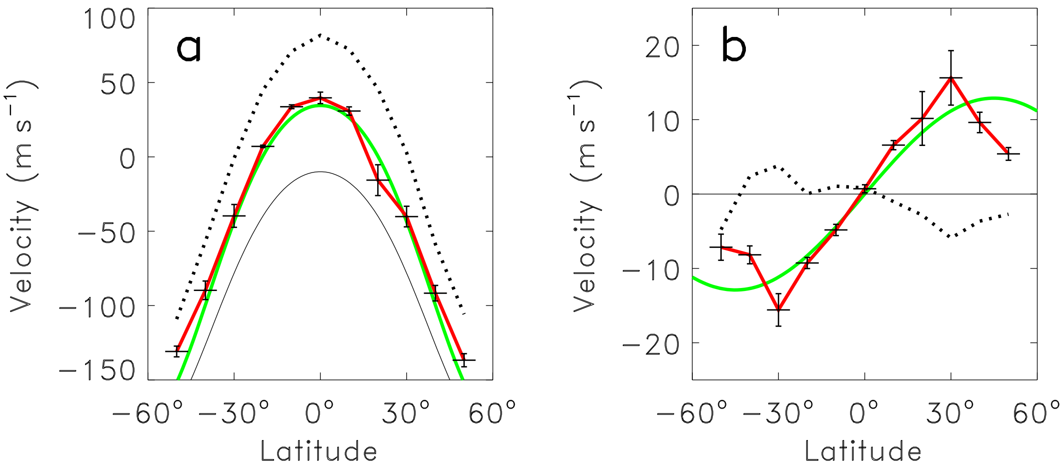

Figure 2.11: Flows, $\boldsymbol{u}$, inferred from the advection of the supergranulation spectrum versus latitude, λ. **(a)** Flow in the direction of solar rotation, u_x (red line and error bars). The green line shows the rotation of the small magnetic features (Komm et al., 1993b) and the black line is for the photospheric rotation (Snodgrass & Ulrich, 1990). The dotted line shows the pattern rotation obtained by tracking supergranular features with a 24 hr delay, in agreement with an earlier measurement (Snodgrass & Ulrich, 1990). **(b)** Northward meridional flow, u_y (red line and error bars). The meridional flow of the magnetic features from Komm et al. (1993c) (green) is again similar. The dotted line shows the anomalous results obtained by tracking the supergranulation pattern with a 24 hr delay. (Gizon et al., 2003)

relationship as it is measured to be independent of both ψ and λ. The data are consistent with a spectrum of travelling waves with a dispersion relation $\nu = \nu_0(k)$. The waves have a rather low quality factor, as can be seen in the azimuthally averaged power spectrum (Fig. 2.12b). The shape of the power spectrum is described accurately by the sum of two Lorentzian functions. From the measured line widths (Fig. 2.12a) we find that the lifetime of supergranules is about 2 days at $l = 100$.[2]

Since ν_0 and the dominant size of supergranules are observed to be essentially independent of latitude, the general dynamics determining the time scale and the spatial scale of supergranulation is not affected by the Coriolis force associated with the large scale vorticity (rotation). We observe, however, a pronounced anisotropy in the azimuthal distribution of wave power at fixed k (Fig. 2.13a). The power is maximum in the direction of rotation and toward the equator in both hemispheres (Fig. 2.13b). The pattern therefore senses the effect of rotation. A snapshot of the

[2]The lifetime is given by $(2\pi \text{ HWHM})^{-1}$ where the HWHM is measured in Hz.

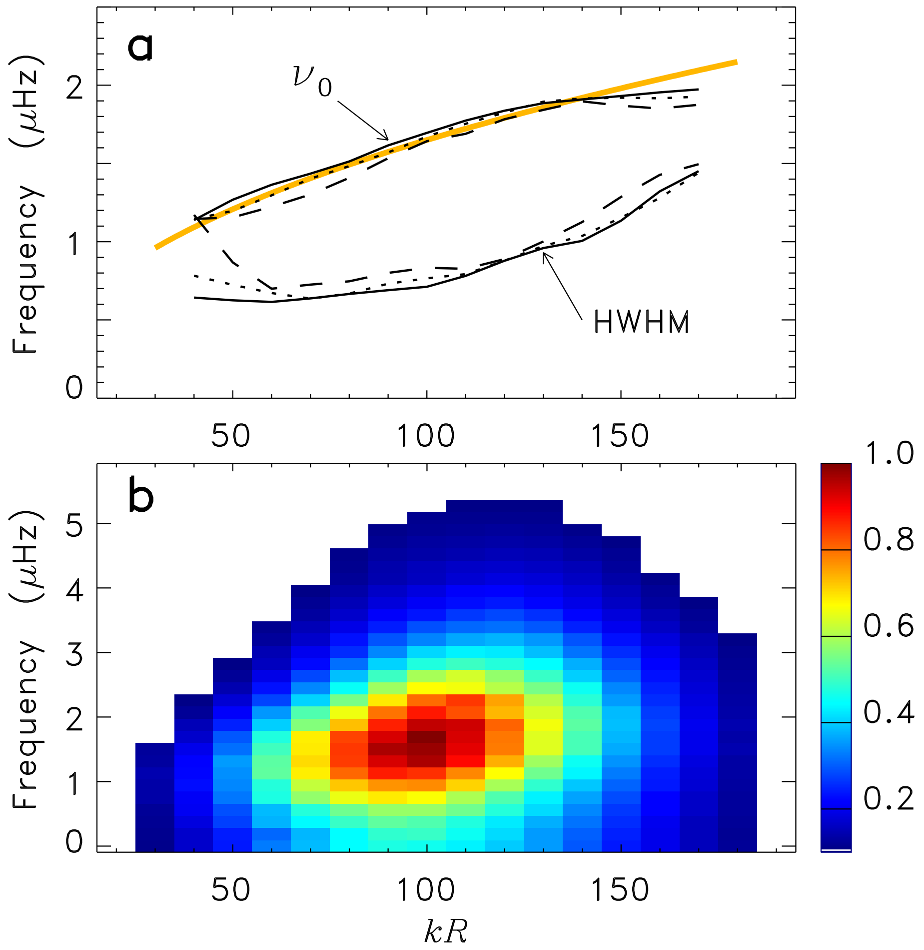

Figure 2.12: Average dynamical properties in a co-moving frame. **(a)** Oscillation frequency ν_0 versus l at latitudes $\lambda = 0°$ (solid), $\lambda = \pm 25°$ (dotted) and $\lambda = \pm 50°$ (dashed). For reference, we plot the approximate dispersion relation $\nu = 1.65(l/100)^{0.45}$ μHz (orange). Also shown is the half width at half maximum (HWHM) of the Lorentzian profiles for the same latitudes, implying an e-folding lifetime of 1-3 days. The quality factor, ν_0/HWHM, does not exceed 2. **(b)** Power spectrum corrected for rotation and meridional circulation and averaged over azimuth and latitude. We note that the distribution of power as a function of frequency is affected only by the known temporal window function, while the wavenumber dependence includes effects of the telescope optics and of the time-distance analysis which are not fully understood. (Gizon et al., 2003)

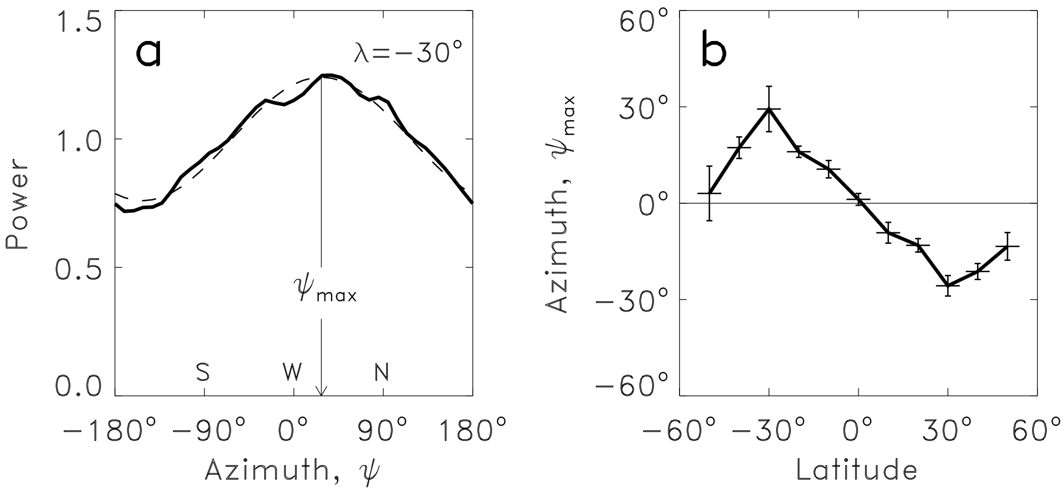

Figure 2.13: Wave power as a function of azimuth and latitude. **(a)** Directional distribution of power at latitude $\lambda = -30°$ (solid line), obtained by integrating $P_k(\nu, \psi)$ over frequencies $\nu > \boldsymbol{k} \cdot \boldsymbol{u}/2\pi$ and then averaging over k. We applied an MTF correction estimated from the data. The azimuth of maximum power, $\psi_{\rm max}$, is measured by fitting a sinusoidal function (dashed line). **(b)** Plot of $\psi_{\rm max}$ versus latitude. There is excess power in the direction of solar rotation and toward the equator in both hemispheres. (Gizon et al., 2003)

divergence field would not reveal this as the sum of the powers measured in opposite directions is nearly isotropic (Fig. 2.13a); the vorticity field, on the other hand, is slightly sensitive to the effect of the Coriolis force as we will show later.

As already mentioned, earlier estimates of supergranulation rotation (Duvall, 1980; Snodgrass & Ulrich, 1990), obtained by tracking the supergranulation pattern from one image to the next, were systematically found to be higher than the rotation of the magnetic network (Fig. 4a). This apparent super-rotation of the pattern can now be understood since waves are predominantly prograde. The East-West motion of the pattern is effectively a power-weighted average of the true rotation and the non-advective phase speed $u_{\rm w} = 2\pi\nu_0/k \sim 65\ {\rm m\,s^{-1}}$. Similarly, the excess of wave power toward the equator is reflected in the meridional motion of the pattern (Fig. 4b).

We have shown that supergranulation displays a high level of organization in space and time. Perhaps this order has its origin in the network of coherent cyclonic plumes that controls solar-like turbulent convection. The prograde excess of wave power is most likely due to the influence of rotation that breaks the East-West symmetry, allowing for new instabilities to propagate. Recent numerical simulations of solar convection (Miesch et al., 2000) show patterns that move prograde relative to the local rotation at low latitudes, and may help explain the observations. Convection in oblique magnetic fields (Hurlburt et al., 1996) also exhibits solutions that take the form of travelling waves, where the tilt of the convection cells, their wave speed, and direction depend on the strength and obliquity of the field. Supergranulation would appear to be a rare known example of travelling-wave convection in a very highly turbulent fluid.

2.3 Effect of the Coriolis Force on Supergranulation

An interesting effect that can be studied with both horizontal components of the flows is the effect of the Coriolis force on convection. This was studied theoretically for a simplified solar convection model by Hathaway (1982). Cellular convection in a rotating incompressible fluid was also studied by Veronis (1959). In these models, the Coriolis force causes divergent and convergent horizontal flows to be associated with vertical components of vorticity of opposite signs. In the northern hemisphere, the cell rotates clockwise where the horizontal divergence is positive, while it rotates counterclockwise in the convergent flow towards the sinks. A corresponding pattern of streamlines is shown in Fig. 2.14. The sense of circulation is reversed in the southern hemisphere and the amplitude is proportional to the radial component of rotation. The vorticity associated with supergranular flows was apparently detected by Kubičela (1973), which is quite remarkable considering the state of technology at that time. The first unambiguous detection of the Coriolis effect is due to Duvall & Gizon (2000). Here we present a more detailled study (Gizon & Duvall, 2003), using the data from the previous section.

As we have seen earlier, f-mode time-distance helioseismology not only provides maps of the horizontal divergence of the flows, but it also provides information about the two individual components of the horizontal velocity (Duvall & Gizon, 2000). We use the data from the previous section to estimate the horizontal vector flow, $\boldsymbol{v} = (v_x, v_y)$, by measuring the difference in travel time for f modes propagating in opposite directions. From each 12 hr vector flow image we subtract the mean image, to remove rotation and field effects. Like before, we consider longitudinal strips centered at latitude λ and $10°$ wide in latitude. The vertical component of the vorticity is given by

$$\mathrm{curl} = \partial_x v_y - \partial_y v_x \ , \tag{2.7}$$

where spatial derivatives are approximated by a first-order centered difference. Note that differential rotation does not contribute to the vorticity as it has been removed. The horizontal divergence of the flow field, denoted by div, can either be obtained

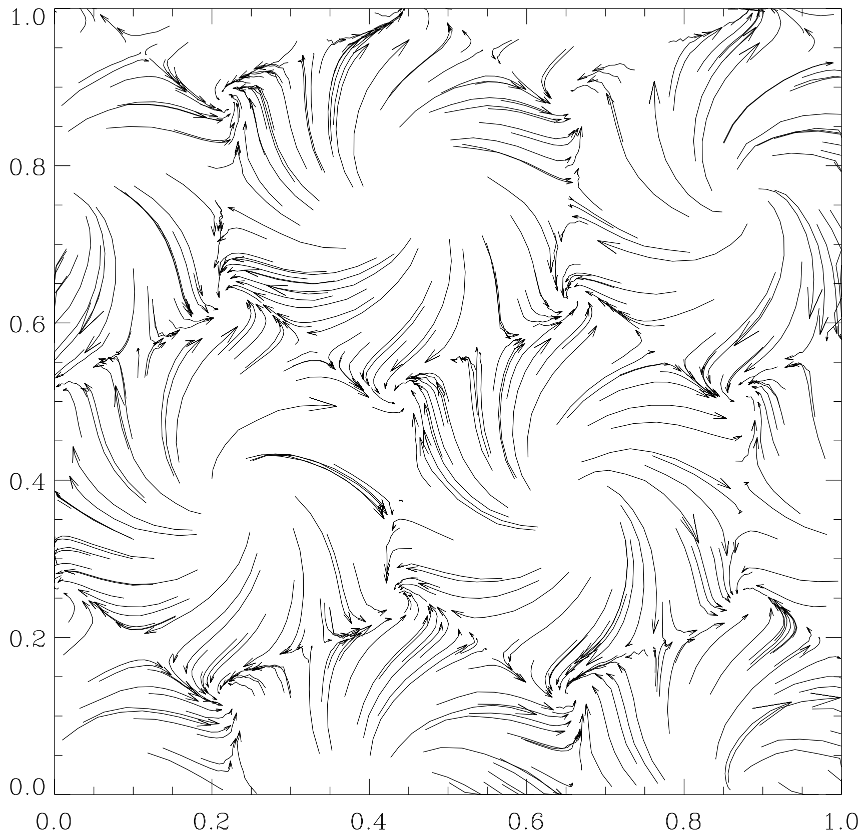

Figure 2.14: A sketch of horizontal streamlines in rotating hexagonal convection cells (Veronis, 1959). The rotation vector is coming out of the page.

by calculating $\partial_x v_x + \partial_y v_y$, or by using the "divergence signal" (difference in travel-times for f modes propagating between a central point and an annulus). In general the second method is preferable as it is less noisy; although both methods compare favorably.

It is not straightforward to predict the statistical properties of the vorticity in rotating turbulent convection (cf. Hathaway, 1982). Vorticity production is due to the effect of the Coriolis force and to vortex stretching and tilting mechanisms. The importance of the Coriolis force is characterized by an inverse Rossby number, or Coriolis number, defined by

$$\mathrm{Co} = 2\tau_{\mathrm{c}}\, \boldsymbol{\Omega} \cdot \hat{\boldsymbol{g}} \ , \tag{2.8}$$

were $\hat{\boldsymbol{g}}$ is a unit vector in the downward direction and τ_{c} is a characteristic correlation time of the turbulence. Linear theory predicts curl $\sim$ Co div (order of magnitude), and we expect the latitudinal variations of the Coriolis effect to go like

$$f(\lambda) = \frac{\Omega(\lambda)\sin\lambda}{\Omega_{\mathrm{eq}}} \ , \tag{2.9}$$

where Ω_{eq} is the equatorial solar angular velocity. Away from the equator, the magnitude of Co is greater than unity in most on the convection zone, except near the surface where it can be very small. Taking $\tau_{\mathrm{c}} = 2$ day we find that $\mathrm{Co} \simeq -0.98 \sin\lambda$ for supergranulation.

Despite the fact that the vorticity field is very noisy, we detect a significant correlation of a few percent between the vertical vorticity and the horizontal divergence (Fig. 2.15a). The correlation coefficient at latitude λ is defined by

$$\mathcal{C}(\lambda) = \frac{\langle \mathrm{div\ curl} \rangle}{\sqrt{\langle \mathrm{div}^2 \rangle \langle \mathrm{curl}^2 \rangle}} \ , \tag{2.10}$$

where the angle brackets denote the spatial average over the area of a 10° band centered around λ. In the North, positive (negative) divergence is correlated with clockwise (anticlockwise) vorticity. The correlation changes sign in the South. The sign and the latitudinal variation of $\mathcal{C}(\lambda)$ are both characteristic of the effect of the Coriolis force on the flows. Away from the equator, the number of right-handed cyclones is not equal to the number of left-handed cyclones.

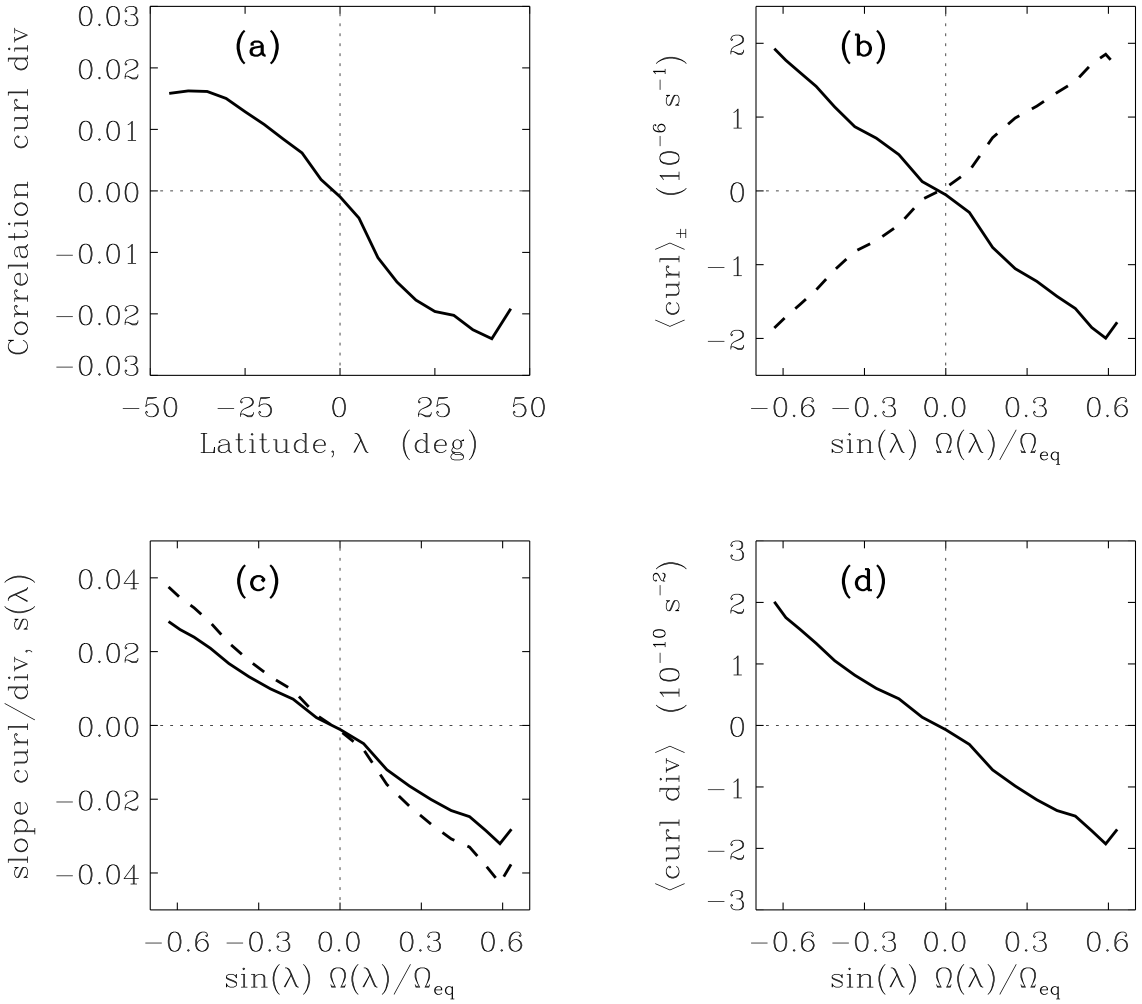

Figure 2.15: Effect of the Coriolis force on supergranular flows. **(a)** Plot of the correlation coefficient, $\mathcal{C}(\lambda)$, between the vertical vorticity, curl, and the horizontal divergence, div. **(b)** Horizontal averages of the vorticity, $\langle \text{curl} \rangle_+$ (solid) and $\langle \text{curl} \rangle_-$ (dashed), over regions with div > 0 and div < 0 respectively. A vorticity of 1 Ms^{-1} corresponds to an angular velocity of 2.5° day^{-1} or a typical circular velocity of 10 $\text{m}\,\text{s}^{-1}$. **(c)** Estimate of the slope, s, in the linear fit curl $= s$ div. The solid line shows $s(\lambda)$ versus $f(\lambda)$ in the case when the ratio of errors $r = \sigma_{\text{div}}/\sigma_{\text{curl}}$ is assumed to be zero. The dashed line is for the case $r = 2$. **(d)** Plot of $\langle \text{curl div} \rangle$ versus $f(\lambda)$.

Figure 2.15b shows horizontal averages of the vertical vorticity, $\langle \mathrm{curl} \rangle_{\pm}$, versus $f(\lambda)$, where the averages $\langle \cdot \rangle_{+}$ and $\langle \cdot \rangle_{-}$ are restricted to the regions of positive and negative divergence respectively. We observe a nearly perfect linear relationship between $\langle \mathrm{curl} \rangle_{\pm}$ and $\mp f(\lambda)$, given by $\langle \mathrm{curl} \rangle_{\pm} \simeq \mp 3 f(\lambda)$ Ms^{-1}. This is again consistent with the interpretation as a Coriolis effect. In principle, a linear fit of the form

$$\mathrm{curl}(\lambda) = s(\lambda)\ \mathrm{div}(\lambda) \tag{2.11}$$

can be extracted from the data at each latitude, λ. This operation is not trivial as it requires a knowledge of the errors in the observations, σ_{curl} and σ_{div}. A first approximation is to assume that div is mostly signal, and curl is mostly noise:

$$s \rightarrow \frac{\langle \mathrm{div\,curl} \rangle}{\langle \mathrm{div}^2 \rangle} \qquad \text{as} \quad r = \frac{\sigma_{\mathrm{div}}}{\sigma_{\mathrm{curl}}} \rightarrow 0\ . \tag{2.12}$$

In this limit we find $s(\lambda) \simeq -0.048\, f(\lambda)$ (Fig. 2.15c), or $s(\lambda) \sim \mathrm{Co}(\lambda)/20$ in terms of the Coriolis number quoted above.

Figure 2.15d shows that the latitudinal variations of the horizontal average $\langle \mathrm{div\,curl} \rangle$ are well described by $\langle \mathrm{div\,curl} \rangle \simeq -3 f(\lambda) \times 10^{-10}$ s^{-2}. This observation may be compared directly to a prediction by Rüdiger et al. (1999), who used the mixing length theory to estimate the effect of rotation on convection:

$$\langle \mathrm{div\,curl} \rangle \sim -\frac{8\alpha^2}{35\gamma^2} \frac{\Omega_{\mathrm{eq}}}{\tau_{\mathrm{c}}}\ f(\lambda)\ , \tag{2.13}$$

where α is the mixing length parameter and γ is the ratio of specific heats. For $\alpha = 1.5$, $\gamma = 5/3$, and $\tau_{\mathrm{c}} = 2$ day, the prediction is $\langle \mathrm{div\,curl} \rangle = -3 f(\lambda) \times 10^{-12}$ s^{-2} for supergranulation, i.e. two orders of magnitude smaller that the measured value. This disagreement is perhaps not too surprising as there is some freedom in choosing α and τ in Eq. (2.13) and the mixing length theory may oversimplify the problem. On the other hand, the measurement errors are not well understood either.

2.4 Large-Scale Flows Around Active Regions

2.4.1 Data Analysis

In this section we use an extensive set of Dopplergrams from the MDI Dynamics Program to construct synoptic maps of the near-surface horizontal flows from measurements of f-mode travel times. The data sets we considered include up to three months of continuous Dopplergrams for each of the years 1996, 1998, and 1999. We recall that in 1996 the sunspot cycle was at a minimum of activity. Regions of size 90° in longitude and 90° in latitude were tracked at the Carrington rotation rate for 24 hr. Images were interpolated onto Postel's azimuthal equidistant projection centered on latitude 0° and Carrington longitude at image center. The tracking procedure is repeated every 20.3 hr so that the Carrington longitude at image center decreases by 12° at each step. Each 24-hr tracked region was then split into three 8-hr data cubes. For each Dynamics period, we thus obtained a sequence of 8-hr data cubes covering two to three months each year. Data cubes go through a three-dimensional Fourier filter to isolate the f-mode ridge and cut off the power below 2 mHz. The temporal signal at a given pixel is cross-correlated with the signal in concentric quadrants of thickness 0.12°. To enhance the signal, cross-correlations are averaged on a 2×2 grid of origins, corresponding to a spatial resolution of 0.24° at image center. West-east and north-south travel time differences are measured by fitting a Gaussian wavelet to the cross-correlations. Travel-times are averaged over a range of annuli with radii ranging from 0.42° to 0.90°. The travel-time perturbations are converted into velocity by using the calibration from section 2.1. In addition, we measure in-out mean travel times. Travel-time maps are then interpolated onto a Carrington longitude-latitude grid with 0.24° resolution in both coordinates.

In order to examine field effects as a source of systematic errors, we construct averages of the flow maps without shifting images with respect to the central meridian longitude. These averages are shown in Fig. 2.16 for rotation and meridional circulation. The small scale fluctuations in theses maps are essentially due to supergranulation. However, at fixed longitude, there are smooth variations as a function of central meridian longitude which cannot be of solar origin. In 1996, the equatorial rotation can vary by as much as ~50 m/s across the 90° longitudinal range (the west

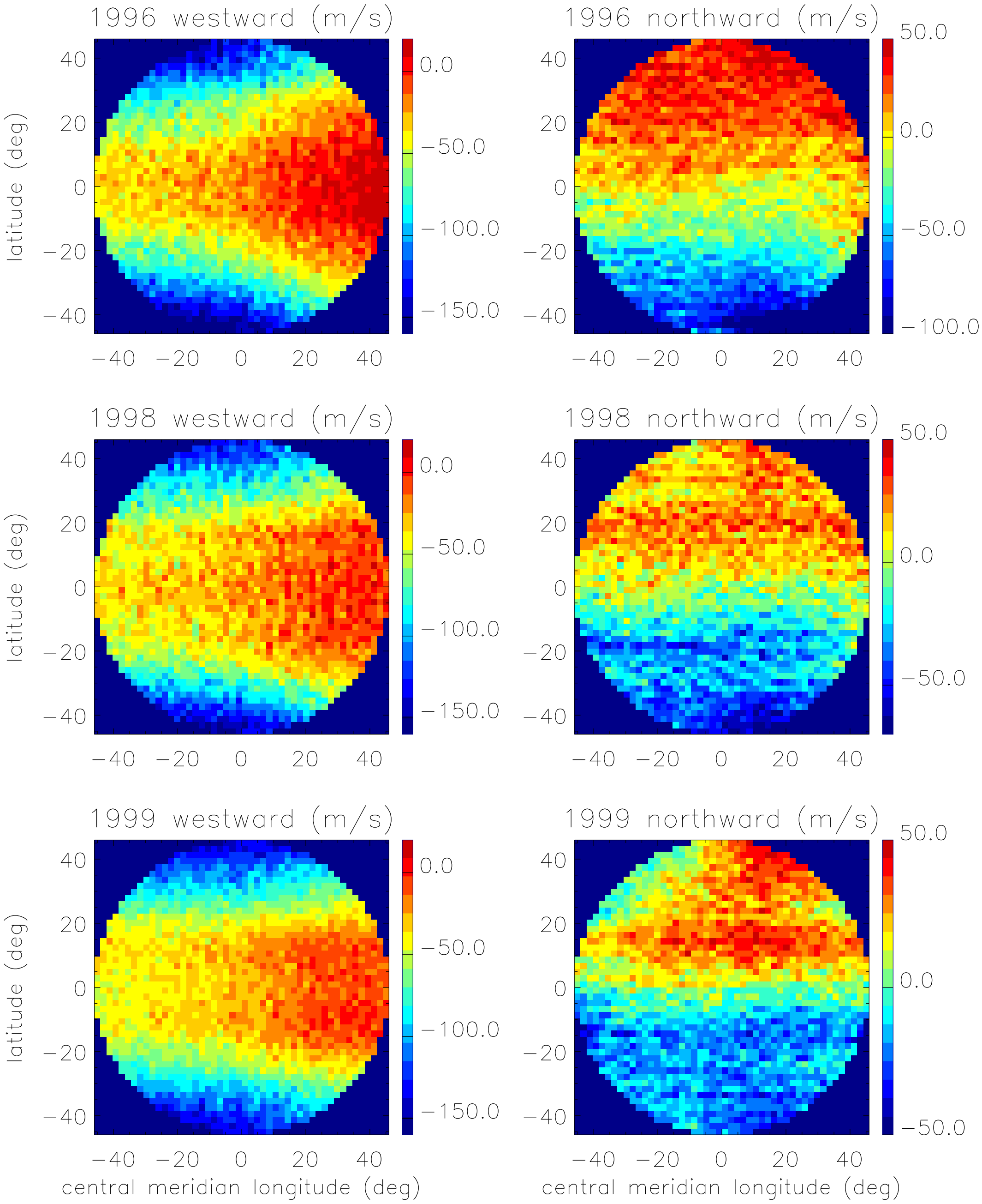

Figure 2.16: Field effects. Average of the maps obtained for the 1999 Dynamics period. The figures on the left are for rotation (measured in a frame corotating at the Carrington angular velocity) and the figures on the right are for meridional circulation. The upper figures are for the 1996 MDI Dynamics run, the middle figures for 1998, and the lower figures for 1999.

limb appears to rotate faster than the east limb). We note that the systematic errors do not appear to be as severe in 1998 and 1999. Field effects can have many possible causes (e.g. point spread function, solar radius error, cubic distorsion, tilt of ccd, plate scale, remapping errors, etc.) and do vary with time (the MDI telescope was, by design, out of focus in 1996 and mostly in focus during 1999). The main causes have not been identified.

2.4.2 Longitudinal Averages

The longitudinal averages of rotation and meridional circulation are plotted in Fig 2.17 for the three dynamics periods. Small offsets were subtracted from the meridional circulation curves to correct for a $0.2°$ P-angle error in the orientation of MDI images (Toner, 2001) and a $0.1°$ error in Carrington's measurement of the inclination of the solar equator to the ecliptic (Giles, 2000).[3] These errors cause solar rotation to leak into the meridional circulation signal with a one year periodicity.

We observe in Fig 2.17 that both rotation and meridional circulation seem to change with time, although we need to keep in mind that there is a time dependence in the systematic errors. Note that poleward meridional motion is not a monotonic function of latitude during periods of magnetic activity (1998 and 1999). In 1998 (resp. 1999) meridional circulation reaches a maximum at latitude $20°$ (resp. $16°$). Other studies reveal a similar behavior (Giles, 2000; Meunier, 1999). As for rotation, it is known from surface Doppler measurements (Howard, 1996) and inversions of global-mode frequency splittings (Schou, 1999) that there are small solar-cycle variations in the rotation rate, known as torsional oscillations or zonal flows. To measure the zonal flows for each dynamics period, we subtract a smooth fit to the angular velocity of the form $\Omega(\lambda) = \Omega_0 + \Omega_1 \sin^2 \lambda + \Omega_2 \sin^4 \lambda$, where λ is the latitude. The north-south symmetric component of the zonal flows is shown in Fig 2.18 (dashed line). The thin solid line shows a previous measurement obtained by Schou (1999) for the same time periods (global modes). The thick solid line shows the zonal flows measured by tracking the superganulation pattern with a correlation tracking technique with $\Delta t = 8$ hr (see Fig 2.9). Figure 2.18 shows a very good

[3] P denotes the position angle of the northern extremity of the axis of rotation, measured eastward from the north point of the disk. The $0.2°$ P-angle error in the pointing of MDI is within specifications.

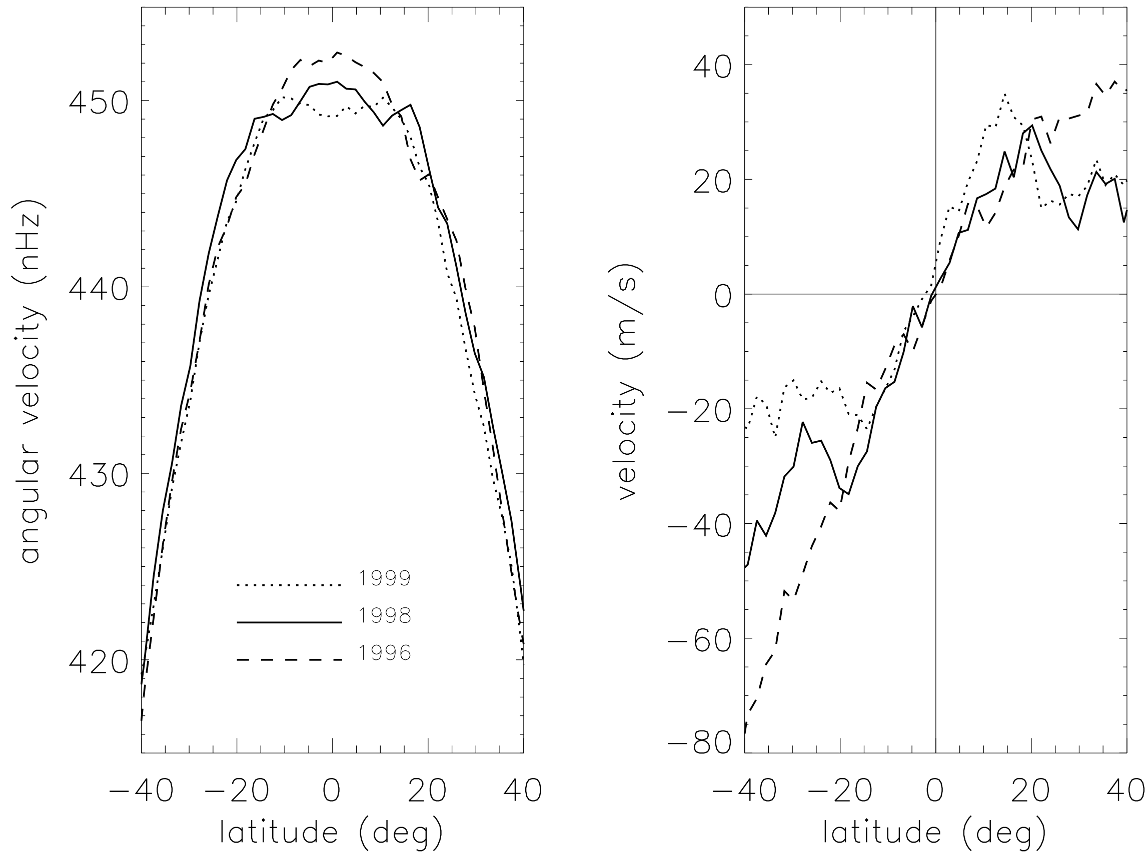

Figure 2.17: Rotation and meridional circulation for the three MDI Dynamics runs of 1996, 1998, and 1999.

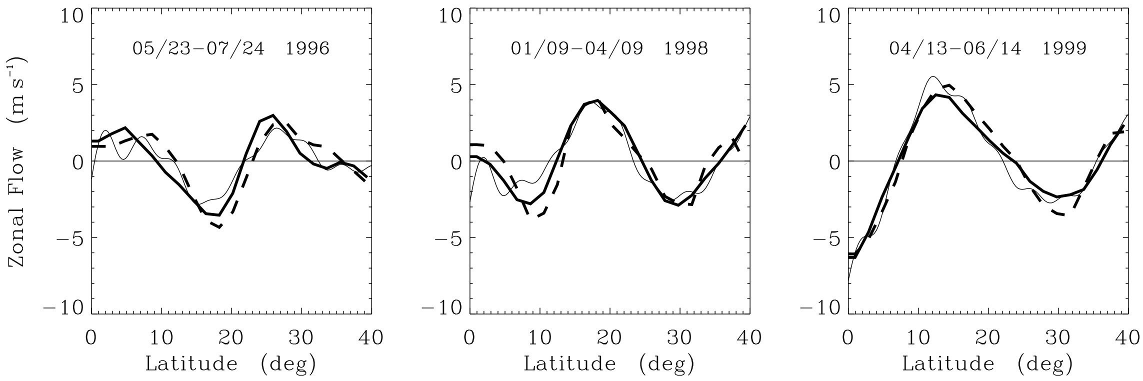

Figure 2.18: North-South symmetric component of the zonal flows obtained after subtraction of smooth rotation curves (thick dashed line, see Fig 2.17). The thick solid line is from correlation tracking of the supergranulation pattern ($\Delta t = 8$ hr, see Fig 2.9). The thin line shows the zonal flows obtained from f-mode frequency splittings (Schou, 1999) for the same time periods.

agreement, in both phase and amplitude, between these three independent methods. This suggests that we are able to measure zonal flows with a very high level of precision, of the order of 1 m/s, and that time-distance helioseismology does work. Because the torsional oscillations vary much faster with latitude ($\sim 20^\circ$ period) than the systematic field effects, we were able to separate the two.

2.4.3 Local Flows

We now investigate the structure of the local flows and their relation to magnetic activity. For a given Dynamics run, we subtract the average flow map (Fig. 2.16) from each individual 8-hr flow map. This enables us to remove all unwanted field effects, and to study residual flows. We then construct synoptic maps by averaging the flows at fixed Carrington longitude. In other words, the maps are averaged in a frame that is corrotating with the Sun at the Carrington rotation rate. This procedure implies that the flows are effectively averaged in time over 7.5 days near the equator; there is less temporal averaging at higher latitudes because individual maps are disks (45° radius, see Fig. 2.16).

Each solar rotation is denoted with a Carrington number. The synoptic residual flow maps are plotted in Fig. 2.19 for Carrington rotation number 1911 in 1996, Fig. 2.20 for Carrington rotation 1948 in 1999, and Fig. 2.21 for Carrington rotation 1949 in 1999. Arrows are plotted every 3.84°. We remind the reader that horizontal flows obtained by f-mode time-distance helioseismology are averaged over the first 2 Mm beneath the photosphere. Also plotted for comparison are MDI synoptic magnetic maps (photospheric magnetic field strength). In addition, we constructed synoptic maps of the mean travel-time perturbations. Mean travel times are obtained by measuring the average travel time for f-modes traveling the distance between a central point and an annulus (inward and outward). Like for the flow maps, we subtracted a background mean travel-time map from each 8-hr map before making the synoptic maps. The mean travel-time perturbations are overlaid on the flow maps.

It is quite clear from the synoptic maps that we detect large-scale flows converging toward active regions. The convergent flows have a magnitude of the order of 30 to 50 m/s and can be detected as far as $\sim 15^\circ$ from a large active center (see

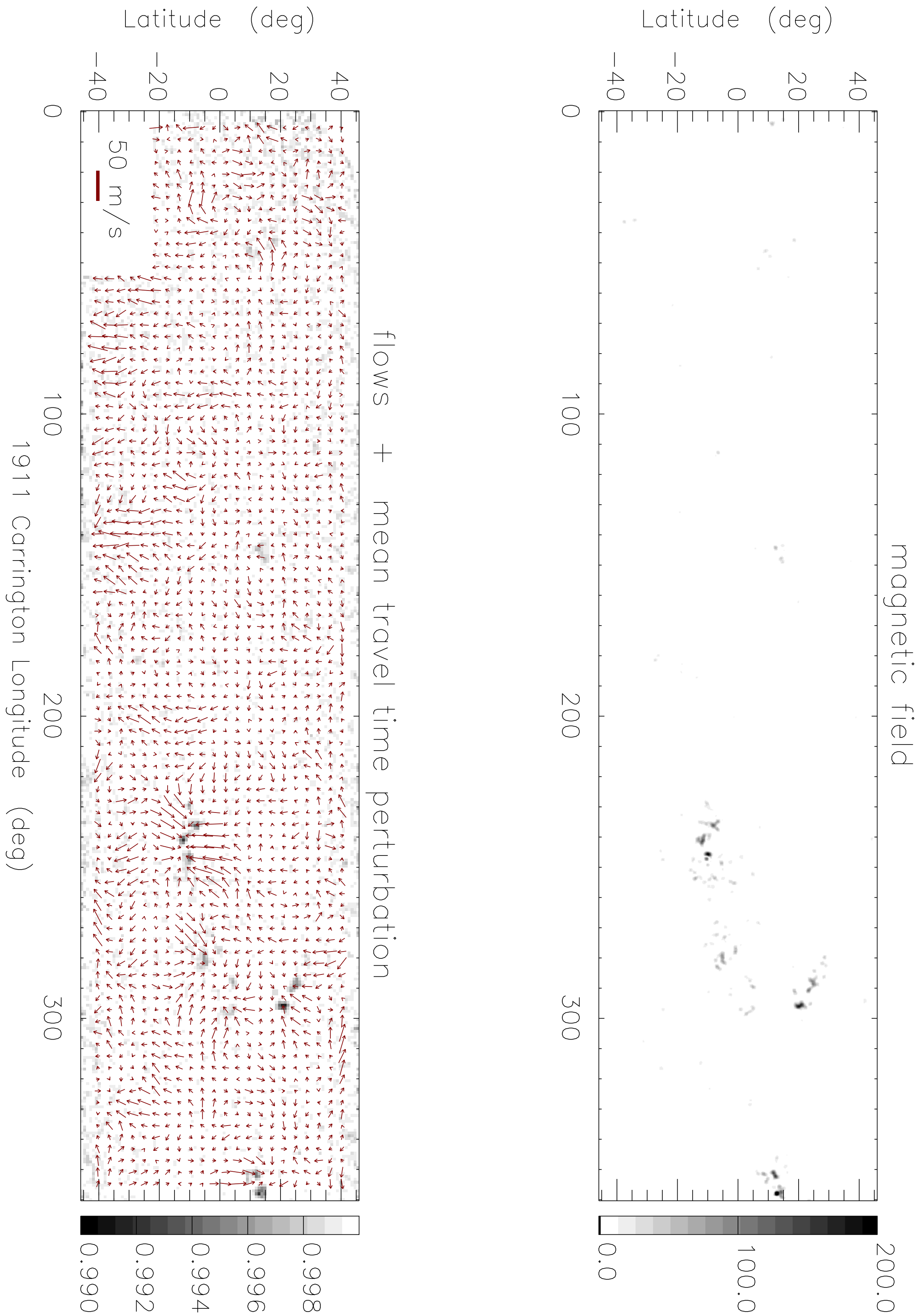

Figure 2.19: Carrington Rotation 1911 (1996). Continuum intensity, magnetic field (Gauss), mean travel time perturbation (normalized), and flow field (absolute magnetic field in the background).

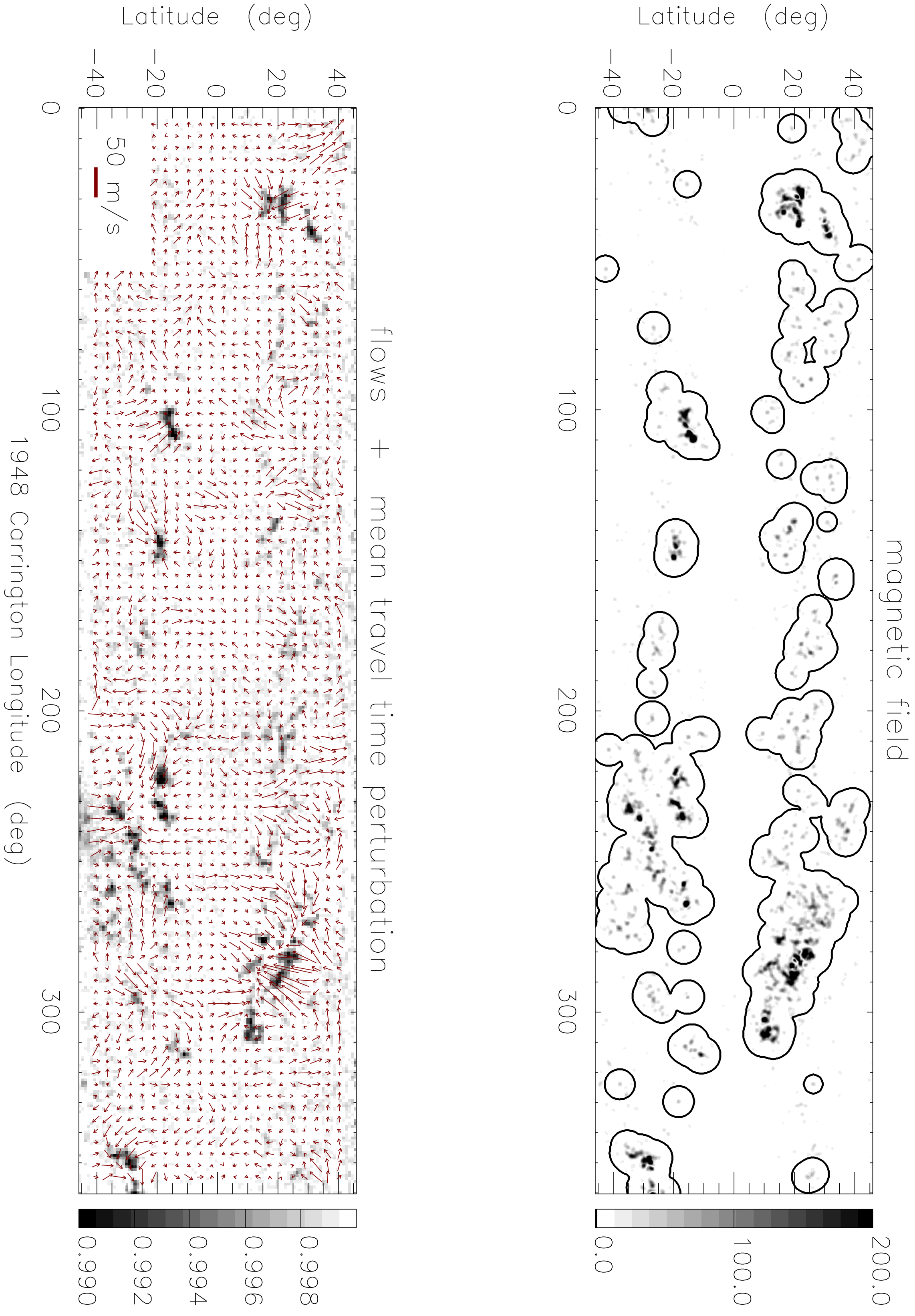

Figure 2.20: Carrington Rotation 1948 (1999)

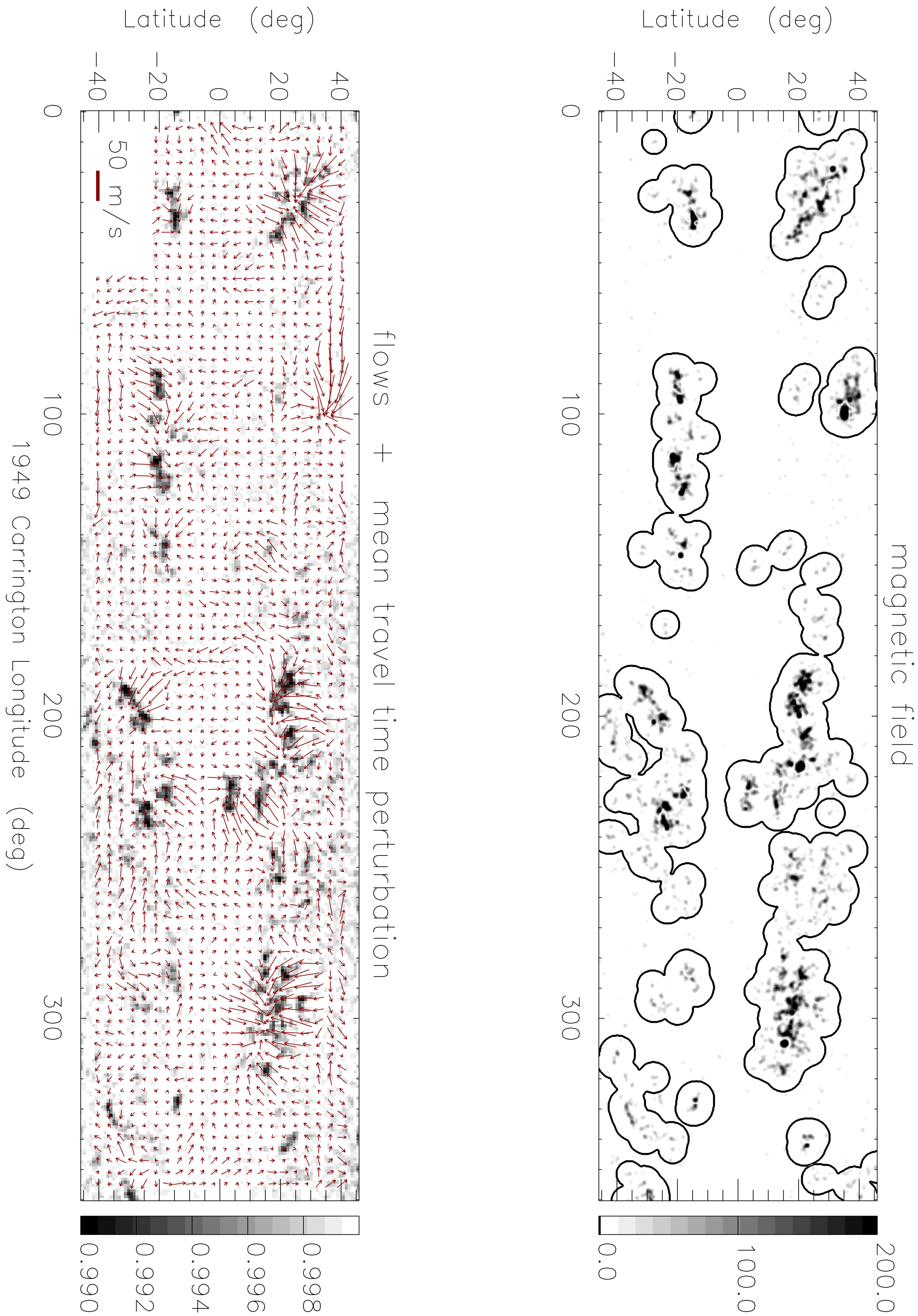

Figure 2.21: Carrington Rotation 1949 (1999)

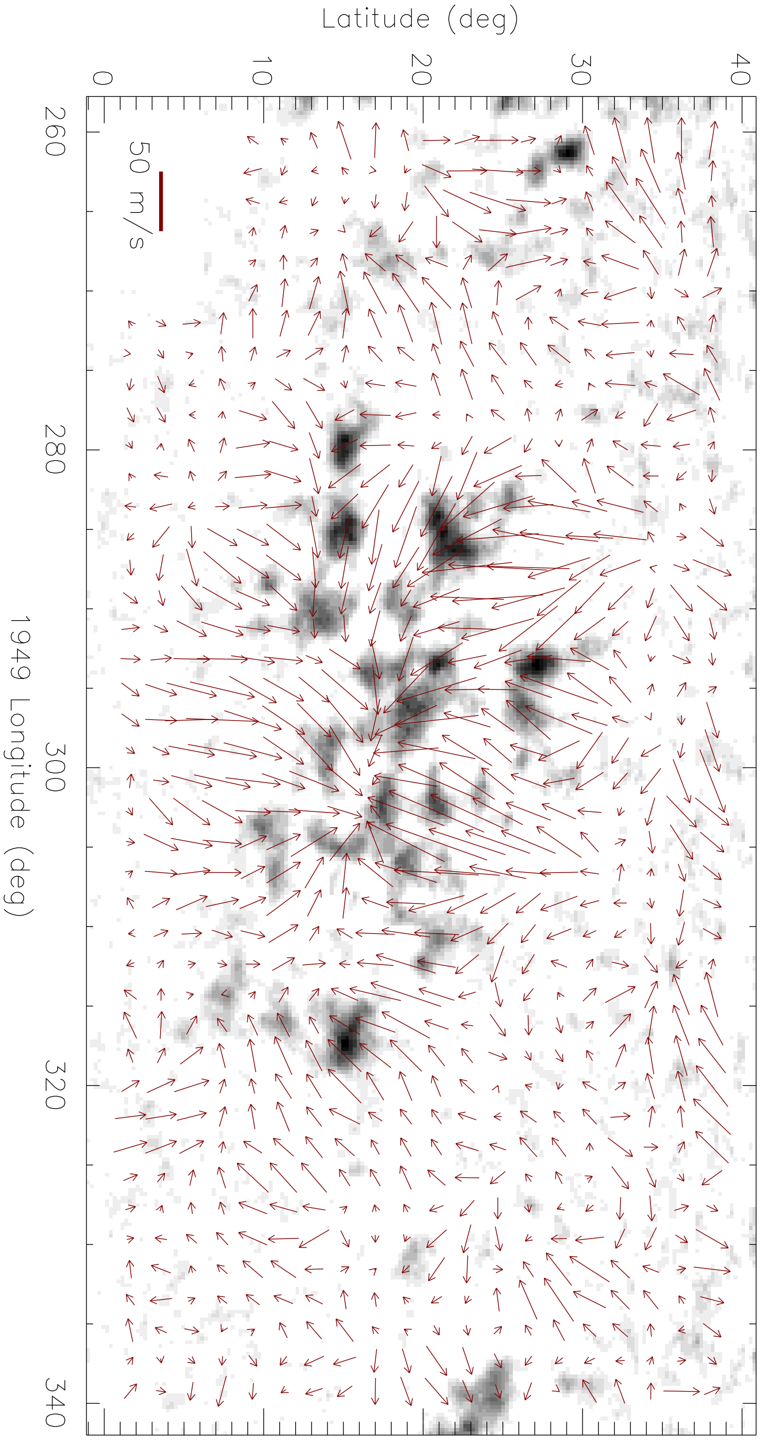

Figure 2.22: Zoom on part of Carrington Rotation 1949 (1999)

Fig. 2.22 for a zoom). Because these flows are small it is important to ask if they are real. Could the travel-time differences be caused by other types of perturbations? This question was first raised by Woodard (1997) who suggested that increased wave damping in active regions could introduce a travel-time difference and therefore mimic a flow. However, both Woodard's analysis and the work presented in chapter 3 imply that travel times should be slightly smaller for waves propagating away from a region of increased damping. Hence this effect cannot be dominant, or we would observe a divergent flow around active regions.

The synoptic maps also reveal that the mean travel-time perturbations are highly correlated with the magnetic field strength: mean travel times are reduced in active regions. This may imply that f-modes travel faster in active regions. Other effects may contribute as well. For instance, if the power spectrum is affected in such a way that high frequency waves have decreased power in active regions then the central frequency of the wave packet would decrease, and the travel-time would decrease as well. The effect of magnetic fields on travel times remains to be studied.

We now come back to the zonal and meridional flows. We have already seen that the longitudinal averages of these flows vary with the solar cycle. An important question is how local flows around large complexes of activity contribute to the longitudinal averages. In order to answer it, we separate the regions of magnetic activity from the quiet regions in Carrington maps 1948 and 1949 (as shown by the contours in Figs. 2.20 and 2.21). Figure 2.23 shows the torsional oscillations and the meridional flows when magnetic regions are excluded from the longitudinal average (thick lines) and when all data are taken into account (thin line). We find that in 1999 the zonal flows are only slightly affected when active regions are excluded from the average. It appears that regions of magnetic activity rotate a little faster. This result was already known (active regions may be rooted beneath the surface where rotation is larger). The active regions are affecting the mean meridional circulation by no more than ± 5 m/s, producing a little kink around the latitude of mean activity. Thus the converging flows around active regions produce a longitudinal modulation in the torsional oscillation. We will come back to this observation later.

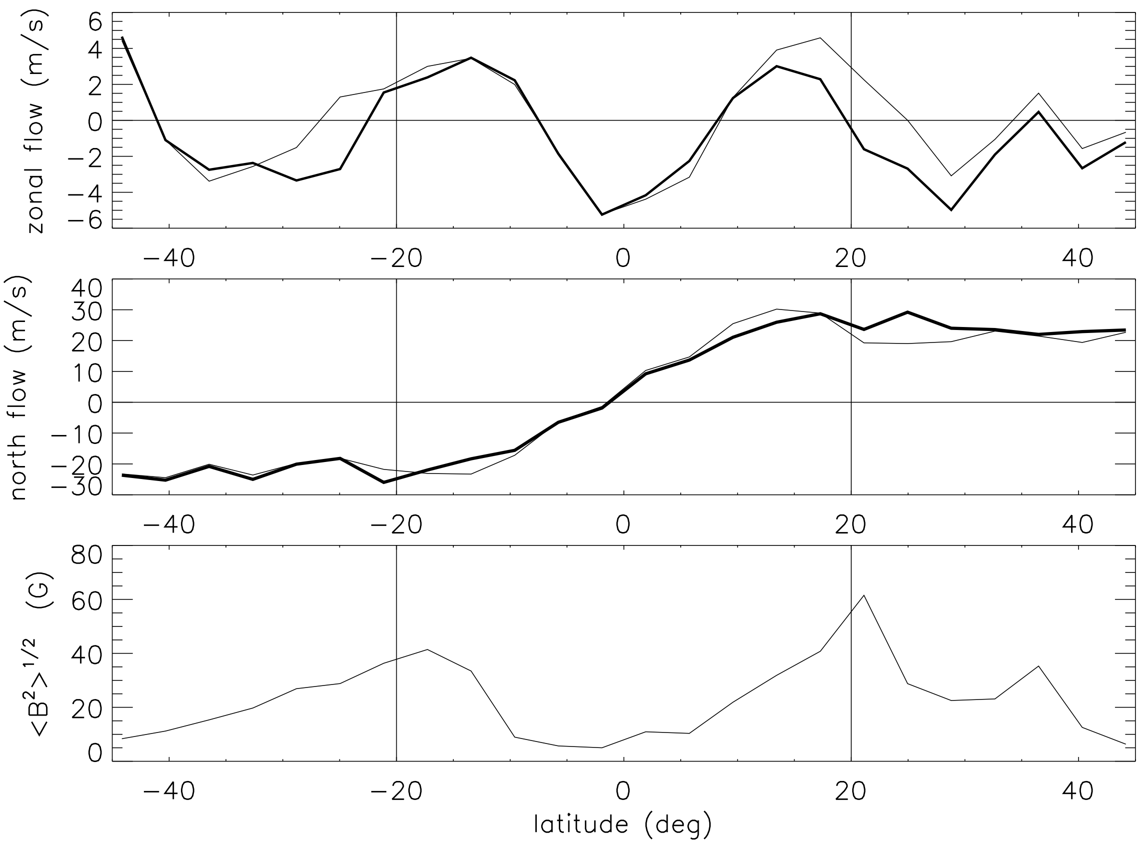

Figure 2.23: Zonal and meridional flows for Carrington rotations 1948 and 1949 in 1999. The thick lines correspond to the longitudinal averages when active regions are excluded from the calculation. The thin lines are averages over the whole maps (quiet and active regions). The bottom panel shows the latitudinal distribution of the magnetic field strength.

2.5 Comparison with Ring-Diagram Flow Maps

In the local helioseismic technique of ring-diagram analysis, a $15^\circ \times 15^\circ$ region of a Doppler image of the Sun is tracked and Fourier transformed in 3 dimensions to obtain a power spectrum. In the presence of flows, waves with the same wavenumber propagating in opposite directions have their frequency split by the Doppler effect. Such frequency splittings are used in ring analysis to measure flow velocities averaged over the depths where the p or f modes have significant amplitudes.

The resulting flow fields display complex and dynamic behavior. At the smallest scales, time-distance has successfully measured supergranular flows (Duvall & Gizon, 2000) and the moat flow around sunspots (Gizon et al., 2000). At larger scales, likely connected to giant cell convection, both the time-distance and ring analysis techniques have now detected strong correlations with magnetic features and near-surface converging flows around active regions. Finally, on global scales, the local techniques have confirmed the presence of the migrating torsional oscillations (e.g. Hathaway et al., 1996; Schou, 1999) and have shown that meridional circulation evolves with the solar cycle (Giles, 2000; Haber et al., 2000; Haber et al., 2002; Beck et al., 2002). Most of this work has been performed independently with little validation of the measurements through comparisons with other techniques. Before, we can fully trust the exciting discoveries of local helioseismology, we must verify that the different local helioseismic techniques are reliable and robust. In this section we make the first direct comparison of flows obtained through ring and time-distance analyses.

Ring analysis assesses the speed and direction of horizontal flows below the solar surface by measuring the Doppler shift of ambient acoustic waves that are advected by the flows. Using the procedures detailed in Haber et al. (2002), the Doppler shifts are measured by careful fitting of the peaks within a 3-D power spectra. Through 1-D RLS inversion of the integral equation which relates the frequency splittings to the flow properties, the horizontal velocity is computed as a function of depth below the photosphere (Hill, 1988; Thompson et al., 1996; Haber et al., 2002). Using Dynamics Program data from MDI, this mode fitting and inversion procedure was applied to different patches on the solar surface on a daily basis to build maps of the local flow field as a function of time and position on the solar disk. Typically, each region consists of a 15° diameter disk. A mosaic of such tiles fills the solar disk out to 60° from the center, with tile centers separated by 7.5° in longitude and latitude. Before analysis, each tile is tracked at the surface rotation rate (Snodgrass, 1984) to remove the effects of differential rotation. The end result is a measurement of the flow field as a function of time, depth, and position on the solar disk. The horizontal resolution is roughly 15° and the vertical resolution is a few Mm near the surface.

Time-distance helioseismology applied to f modes provides information about the two components of the horizontal flows in a 1 Mm-deep layer beneath the surface (§ 2.4). These time-distance flow maps are sampled every 0.24°. For comparison with the ring analyses which have far coarser resolution, the resolution of the time-distance measurements has been degraded by spatial averaging. The averaging was performed over each of the 15° diameter tiles in the ring-analysis mosaic, and the flows were weighted by the spatial apodization function used to generate the 3–D spectra employed in the ring analysis. The end result is a set of measurements with the same coverage and horizontal resolution as the ring-analysis. Figure 2.24 shows synoptic maps of the residual flow field that remain after the longitudinal mean has been removed from both the time-distance and ring-analysis flows. Figure 2.25 shows the longitudinal means of the zonal and meridional flows for both techniques. The data are for the Carrington rotation 1948 (1999).

The residual flows obtained using the time-distance and ring analysis methods agree remarkably well. Subtle differences do appear in the flow details. However, centers of outflow and inflow as well as flow directions are largely identical in the synoptic maps obtained using either technique. In particular, the inflows located around magnetic active regions are captured by both methods. The Spearman rank correlation coefficient between the two sets of residual flows is roughly 0.8 for the Carrington rotation shown in Fig. 2.24. In comparison, correlations made between the time-distance measurements for one Carrington rotation and the ring analysis measurements for a different rotation generally produce a coefficient with a modulus less than 0.1. The correlation is highest when the depth used for the ring analysis is roughly 1 Mm, the height best sampled by the f modes used in the time-distance analyses. The correlation begins to drop precipitously as the depth increases beyond 2 Mm, dropping to as low as 0.4 at a depth of 16 Mm.

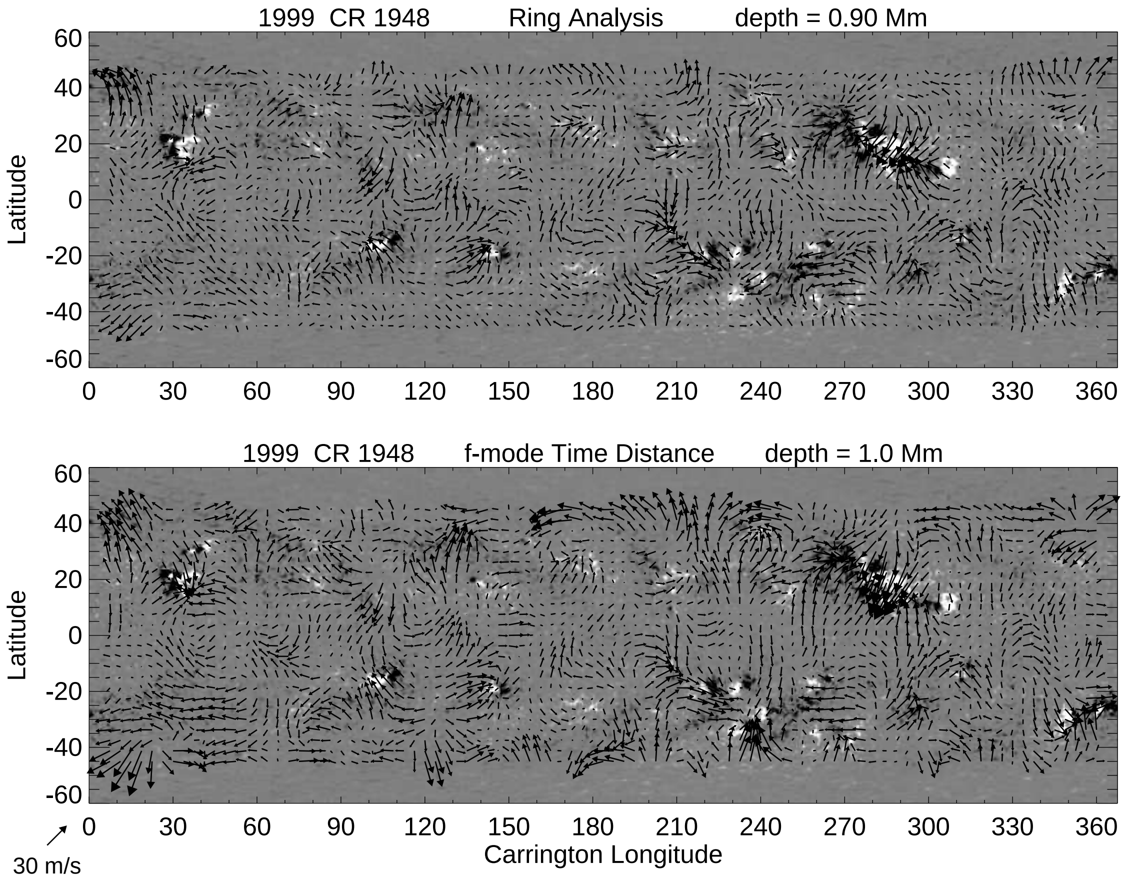

Figure 2.24: Synoptic maps of near-surface flows for Carrington rotation 1948 spanning 3 Apr – 29 Apr 1999. The flow field shown is the residual that remains after the mean meridional and zonal flows have been subtracted. The upper map was obtained using ring analyses with RLS inversion. The lower map was generated from time-distance analyses of f-mode data without depth inversion. The time-distance measurements have been averaged spatially such that the two analysis schemes have the same horizontal resolution of 15°. The tiles used in the ring analyses overlap by 7.5°, and the resulting flow field has been interpolated twofold to generate arrows with a spacing of 3.75°.

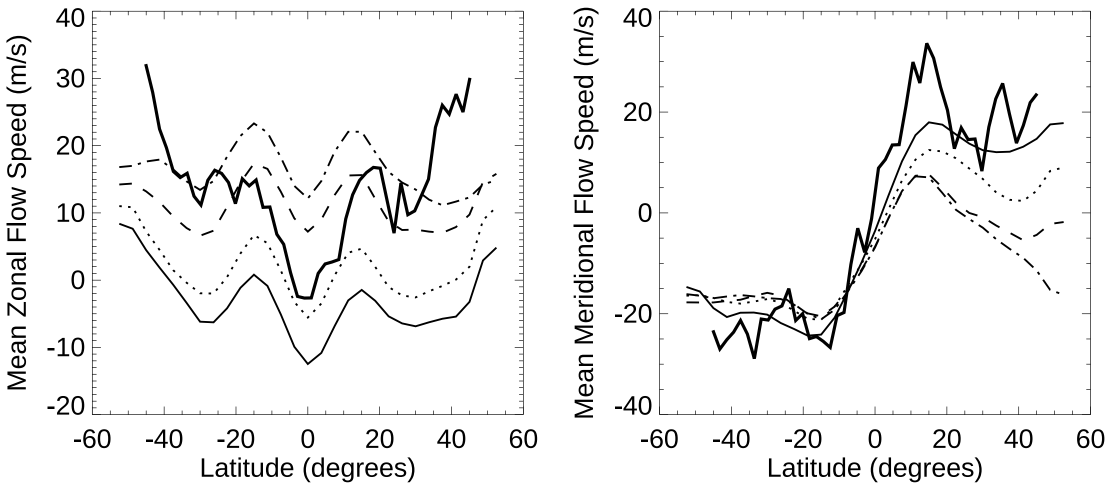

Figure 2.25: The mean zonal flows (left panel) and meridional flows (right panel) as a function of latitude obtained using ring analysis and time-distance f-mode analysis of Dynamics Program data from Carrington rotation 1948 (in 1999). The zonal flow is measured relative to the surface differential rotation rate of Snodgrass (1984). The thick solid curve is the flow obtained with time-distance analysis. The other curves were obtained using ring analysis, and correspond to the flow at different depths: solid 0.9 Mm, dotted 2.0 Mm, dashed 4.4 Mm, and dot-dashed 7.1 Mm. These flows were removed from the full flow field to obtain the synoptic map shown in Fig. 2.24.

In contrast, the mean flows display less similarity. Both techniques generate zonal flows that have consistent shape as a function of latitude. However, there appears to be a substantial constant offset of 15 m/s between the rotation rates. This offset represents about 0.8% of the sun's equatorial rotation rate. We do not fully understand the source of this offset, although we suspect that it is due to the different tracking and remapping methods used to remove rotation and sphericity. The time-distance analyses for a given day are performed on a single region, 90° square, that is tracked at the Carrington rate and remapped using an equal area projection. The ring analysis is executed on many different regions each 15° in diameter, each tracked at the local surface differential rotation rate and remapped using Postel's projection. The mean meridional flows obtained by both techniques and shown in Fig. 2.25 are roughly consistent when the time-distance results are compared to the 0.9 Mm depth of the ring analysis measurements.

The similarities between the residual flows obtained with f-mode time-distance and ring analysis are heartening. Both techniques appear to provide reliable measurements of large scale flows just beneath the solar surface.

2.6 Solar-Cycle Variation of the Meridional Flows

We construct maps of rotation and meridional flows using time-distance helioseismology applied to p modes from the MDI Structure Program. The mean travel distance is 17° corresponding to a maximum depth of 65 Mm below the surface (no depth inversion is done). Meridional flow maps show a time-varying component that has a banded structure with an equatorward migration over the solar cycle. The time-varying component of meridional flow consists of a flow diverging from the dominant latitude of magnetic activity. This map is compared with torsional oscillation maps and with magnetic strength maps, showing a correlation with active latitudes and a strong link between the time-varying component of the meridional flow and the east-west torsional oscillations.

2.6.1 Introduction

Torsional oscillations and meridional flows have been studied for over two decades (e.g. Howard & LaBonte, 1980; Duvall, 1979; Ulrich, 1988). The surface meridional flow is generally agreed to be poleward in both hemispheres with an amplitude of 10-20 $\mathrm{m\,s^{-1}}$. The torsional oscillations (also termed 'zonal flows') consist of latitudinal bands of alternating faster and slower rotation which migrate toward the equator over the solar cycle and are superimposed on top of the differential rotation. The zonal flows can be seen at depths of 56 Mm (Howe et al., 2000) with global helioseismology.

Meridional flows have been difficult to measure by direct Doppler observation due to their small amplitude compared to the large amplitude velocity patterns such as convective limb shift and rotation. However, Nesme-Ribes et al. (1997) have studied meridional flows using sunspots as tracers and have identified a correlation of east-west and north-south motions consistent with angular momentum transport which would sustain differential rotation. Time variations of the meridional flow were noticed by Ulrich (1988) and Hathaway (1996).

The p-mode time-distance helioseismology studies of the meridional circulation conducted by Giles et al. (1997) and Giles (2000) showed that it extends through the convection zone. Haber et al. (2002) studied meridional flows using ring-diagram analysis and found indications of a second meridional cell during the years 1998 through 2001 in the outer 7 Mm; additionally, they found an asymmetry in the meridional flows between the northern and southern hemispheres which would have impact on angular momentum transport. Chou & Dai (2001) studied subsurface meridional flows using time-distance helioseismology and found a time-varying component which extends down to 70 Mm. They suggested that the varying flow could be linked to magnetic activity. Furthermore we showed in Sec. 2.4 that, near the surface, meridional circulation is affected by large-scale convergent flows around active regions.

2.6.2 Analysis and Results

The data reduction followed the description by Giles (2000). The data spanned from May 1996 through July 2001 and consist of medium-resolution MDI dopplergrams. The data gap from June 1998 until March 1999 corresponds to the period of broken contact with SOHO. Images were grouped into 72-hour periods for detrending of solar rotation and supergranulation. Regions, spanning 100° in latitude and longitude, were tracked at the solar rotation rate. These tracked regions were 'stacked' into a data cube for further processing, which consisted of applying a high-pass filter (cutoff at 1.7 mHz) to remove supergranulation and applying a phase-speed filter to select acoustic modes. Temporal cross-correlations were obtained using code developed by Giles (2000). To measure meridional flows, cross-correlations are computed between pairs of points separated in latitude by amounts ranging from 3° to 45°. To improve the signal-to-noise ratio, the cross-correlation functions for each latitude were averaged over three-month periods. Further averaging was done keeping the mid-point constant, and producing 61 latitude bins ($\sim 3°$ sampling). This was repeated for 21 three-month epochs. This procedure was also performed in an east-west direction to measure rotation.

Wave travel times were measured by fitting to the cross-correlation function. A positive time delay corresponds to a flow to the north in the case of meridional circulation or a flow to the west for rotation. The measurement of the travel-time shifts follows closely the method discussed by Gizon & Birch (2002). At each distance, a mean reference cross-correlation symmetric for the two senses of time

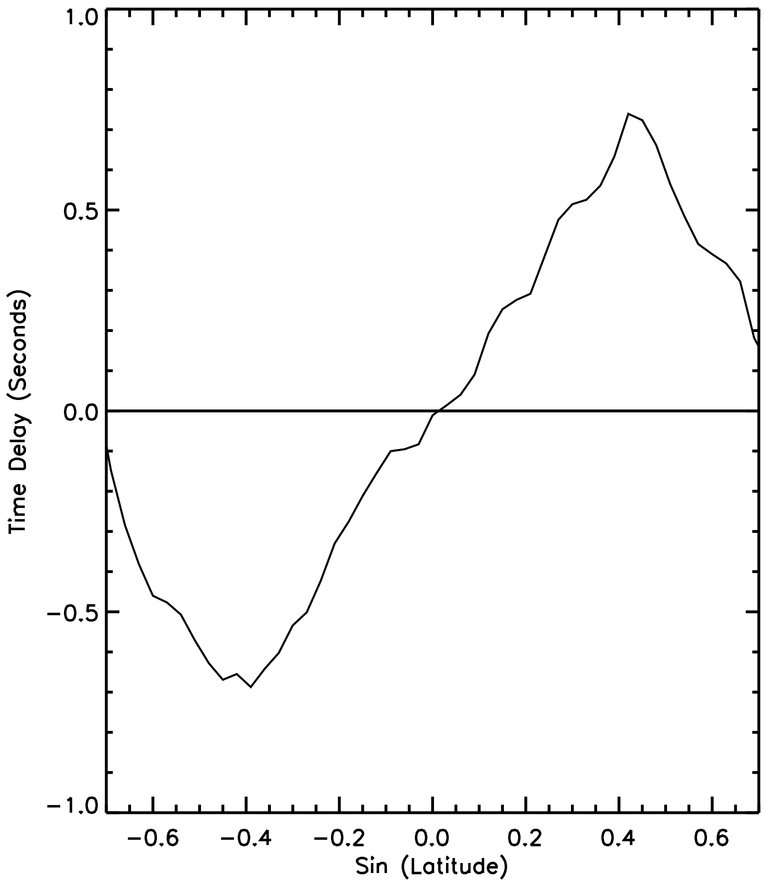

Figure 2.26: Mean meridional flow. The mean signal of meridional flows is shown here for the interval May 1996-July 2001. A northward flow corresponds to a positive travel-time shift. From a simple meridional flow model (Giles, 2000), we estimate that a 1 s time shift corresponds to $\sim 20\ \mathrm{m\,s^{-1}}$.

lag was derived. This reference function was cross-correlated with an individual cross-correlation to yield an approximately zero-centered result except for the shift away from zero due to the flow. A weighted average over distances was derived with the contribution peaked near a distance of 17° with a width of 4°. A ray connecting points separated by 17° extends to a depth of 65 Mm. The time shift was measured as twice the shift of the maximum of this correlation away from zero lag by forcing a parabola through the three closest points to the peak. The factor of two is necessary to match earlier definitions of time shift which involved measuring the shift of positive time lags and negative time lags separately and taking the difference, effectively doubling the signal.

As shown in Fig. 2.26, the meridional flow averaged over time is strongly antisymmetric as a function of latitude, with positive values indicating a northward flow. The peak velocity is about 15 $\mathrm{m\,s^{-1}}$ toward the poles at mid-latitudes. Small errors in the pointing of the MDI telescope can cause solar rotation to contaminate meridional velocity measurements. Taking the antisymmetric component removes this error. The time-varying component of the meridional flow was obtained by subtracting a smooth fit to the 5-year average from the measurement at each epoch. Figure 2.27a shows the residuals, with red indicating poleward motion in both hemispheres. The east-west flow was similarly analyzed, with the exception that a smooth rotation curve was subtracted to produce the torsional oscillation pattern shown in Fig. 2.27b. Torsional oscillations obtained from f-mode frequency splittings by Schou (1999) are shown for comparison in Fig. 2.27c.

A map of magnetic field strength is included in Figure 2.27d to indicate the active latitudes over the period of interest. To compare with the flow maps, a mean latitude of magnetic activity was derived by taking the absolute value of the magnetic field (from MDI synoptic charts), re-binning in latitude and longitude, symmetrizing in latitude, squaring, and fitting a Gaussian function in latitude at each longitude. The mean latitude of activity, given by the location of the peak of the Gaussian, is plotted on top of the velocity maps in Figure 2.27 to indicate the strong connection between the magnetic cycle and the equatorward propagating flow patterns.

The flows are organized about the mean latitude of magnetic activity. The residual meridional flow is away from the latitude of activity. Whether the residual flows cause the magnetic activity to emerge at this latitude or is a result of rising magnetic flux is unknown. The zonal flow is faster equatorward of the mean latitude of activity and slower poleward, as noted previously by LaBonte & Howard (1982). The time-varying component of the meridional flow correlates very well with the zonal flows, with a more strongly poleward flow corresponding to a slower rotation. Although we have not derived the depth dependence of the flows explicitly, the north-south component of the "torsional oscillation" that we detect is tens of megameters beneath the surface (65 Mm maximum). What is not known yet is the longitudinal structure of the residual flows.

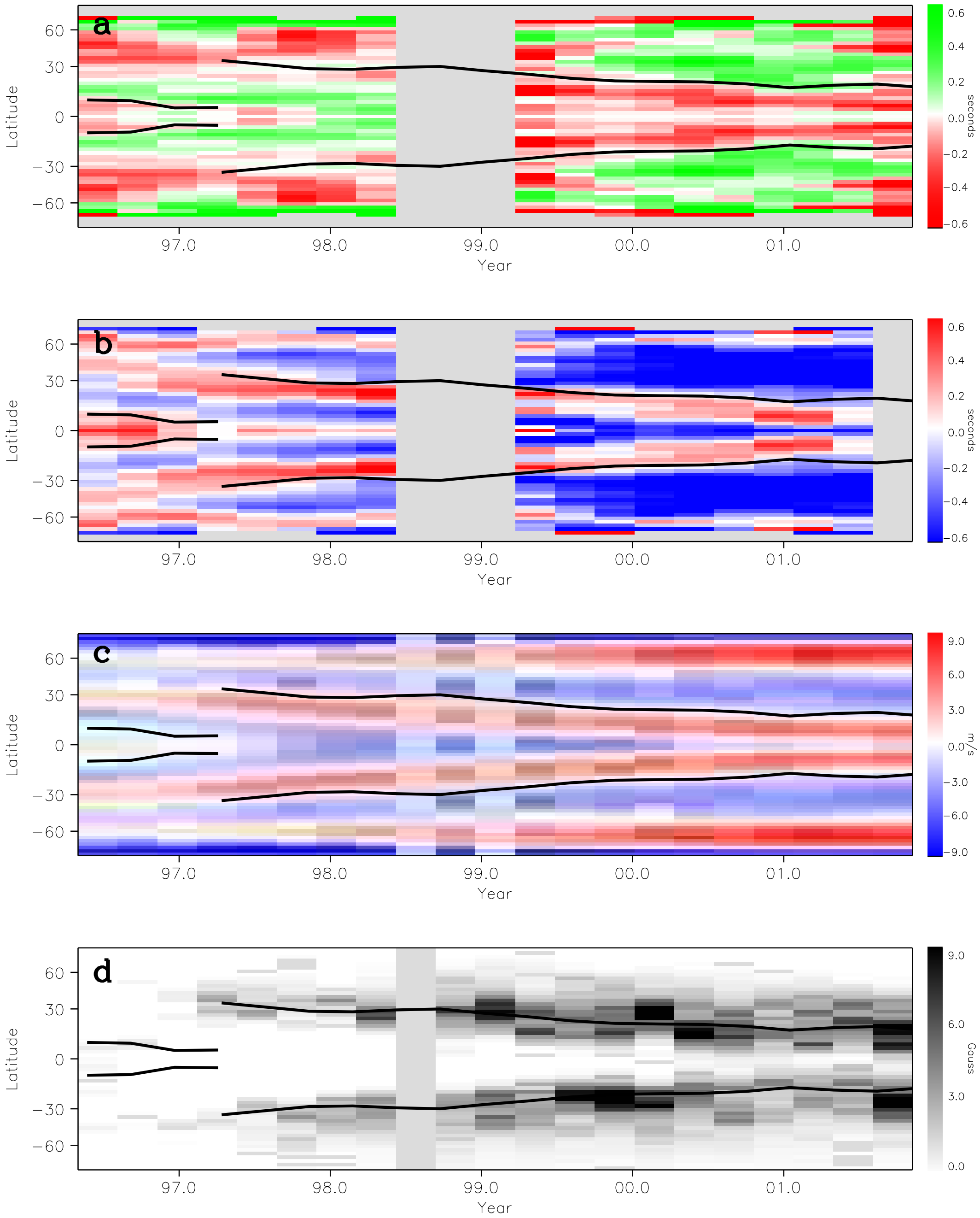

Figure 2.27: Residual meridional flow and torsional oscillation maps from time-distance helioseismology compared with a torsional oscillation map from global modes and a butterfly diagram of magnetic fields. The heavy black line over-plotted is the mean latitude of activity. a) The poleward flow, obtained from subtracting a fit to the mean meridional flow and symmetrizing the residuals. A positive time delay indicates a poleward flow in both hemispheres. b) The torsional oscillations obtained from time-distance helioseismology. Red is prograde. c) Torsional oscillations obtained from f-mode frequency splittings (Schou, 1999). d) Magnetic field strength derived from MDI synoptic charts.